AGU PUBLICATIONS

JGR

Journal of Geophysical Research: Atmospheres

RESEARCH ARTICLE
10.1002/2016JD025933

Key Points:
- Small electrical discharges typically occur continually at low rates in the overshooting tops of storms
- The maximum altitude of discharges in an overshooting top correlates well with the maximum altitude of 18–30 dB*Z* radar reflectivity
- Periods with sustained rates of discharges in overshooting tops tend to have more dangerous weather

Correspondence to:
D. R. MacGorman,
don.macgorman@noaa.gov

Citation:
MacGorman, D. R., M. S. Elliott, and E. DiGangi (2017), Electrical discharges in the overshooting tops of thunderstorms, *J. Geophys. Res. Atmos.*, *122*, 2929–2957, doi:10.1002/2016JD025933.

Received 13 SEP 2016
Accepted 16 FEB 2017
Accepted article online 19 FEB 2017
Published online 8 MAR 2017

Electrical discharges in the overshooting tops of thunderstorms

Donald R. MacGorman[1,2], Matthew S. Elliott[2,3], and Elizabeth DiGangi[2,3]

[1]NOAA/National Severe Storms Laboratory, Norman, Oklahoma, USA, [2]Cooperative Institute for Mesoscale Meteorological Studies, University of Oklahoma, and NOAA/OAR/NSSL, Norman, Oklahoma, USA, [3]School of Meteorology, University of Oklahoma, Norman, Oklahoma, USA

Abstract Previous studies have found that the vertical distribution of sources of very high frequency (VHF) signals from discharges mapped by Lightning Mapping Arrays typically have a secondary maximum in a storm's overshooting top. Low rates of these sources tend to occur continually throughout the lifetime of the overshooting top (OT), rather than sources occurring in the episodic distinct flashes observed at lower altitudes. This study examines the evolution of the VHF OT signature (VHF OT, defined here as a sustained period of ≥4 VHF sources per minute per 200 m layer above a storm's level of neutral buoyancy (LNB)) relative to the evolution of radar reflectivity and IR imagery of overshooting tops in three supercell and two multicell storms. The VHF OT began before OTs were detected in IR satellite imagery of the supercell storms. No OT was observed in IR imagery for either multicell storm, but this lack may have been due to the spatial and temporal resolution of the current IR imager. The VHF OT began near the time the 18 or 30 dB*Z* echo top rose above the LNB and ended near the time it fell below the LNB. There were too few radar volume scans of OTs in the multicell storms for a correlation analysis. In the supercell storms, however, the maximum altitude of VHF sources typically was less than or equal to the altitude of 18 dB*Z* echo tops and was correlated with these echo tops (linear correlation coefficient ≥0.86) during the period of the VHF OT.

1. Introduction

Several studies have observed that VHF sources detected by lightning mapping systems extend above the level of neutral buoyancy (LNB) in overshooting tops penetrating the stratosphere during strong updraft pulses [*Krehbiel et al*., 2000; *Ushio et al*., 2003; *MacGorman et al*., 2008; *Bruning et al*., 2010; *Emersic et al*., 2011; *Calhoun et al*., 2013]. Although neither *Lhermitte and Krehbiel* [1979] nor *Ushio et al*. [2003] indicated the height of the LNB, both noted that the top of successive pulses of larger densities of VHF sources could rise from middle levels of storms to 14 km mean sea level (msl) or more, typically at speeds of 8–20 m s^{-1}. Lhermitte and Krehbiel noted that the VHF maxima rose at the speed of new updrafts inferred from triple Doppler radars. Ushio et al. also suggested that each successive surge was from a new updraft pulse and noted that one pulse could begin while another was reaching upper levels of the storm, with successive beginnings of pulses being separated by roughly 5 min or more. As noted by *Emersic et al*. [2011] in a study of a multicell severe hailstorm and by *Calhoun et al*. [2013] in a study of a supercell thunderstorm, these VHF sources penetrated the overshooting top of the storms and consistently formed a secondary maximum in the vertical distribution of sources of VHF radiation.

Both of these last two studies reported that the character of discharges in the overshooting top is unusual in that the VHF sources usually occur continually at relatively low rates, without discernable channel structure (i.e., probably have very small spatial extent), independent of flashes at lower altitudes, for periods up to a few hours (roughly as long as the overshooting top exists). As illustrated in Figure 1, such behavior is in contrast to a traditional lightning flash, which is a few kilometers to >100 km in horizontal extent and typically produces a burst of tens to thousands of mapped VHF sources from lightning channels lower in the storm over a time period on the order of 1 s or less. Sequential flashes are typically separated by ≥200 ms or by at least several kilometers. In the storm studied by *Calhoun et al*. [2013], the continual high discharges typically filled much of the region within the 15 dB*Z* reflectivity contour of the overshooting top.

The present study examines VHF sources relative to radar reflectivity and satellite imagery of the overshooting top and relative to severe weather. As will be shown, the timing and maximum height of VHF sources in overshooting tops compare well with the timing and height depicted by radar reflectivity, but VHF mapping

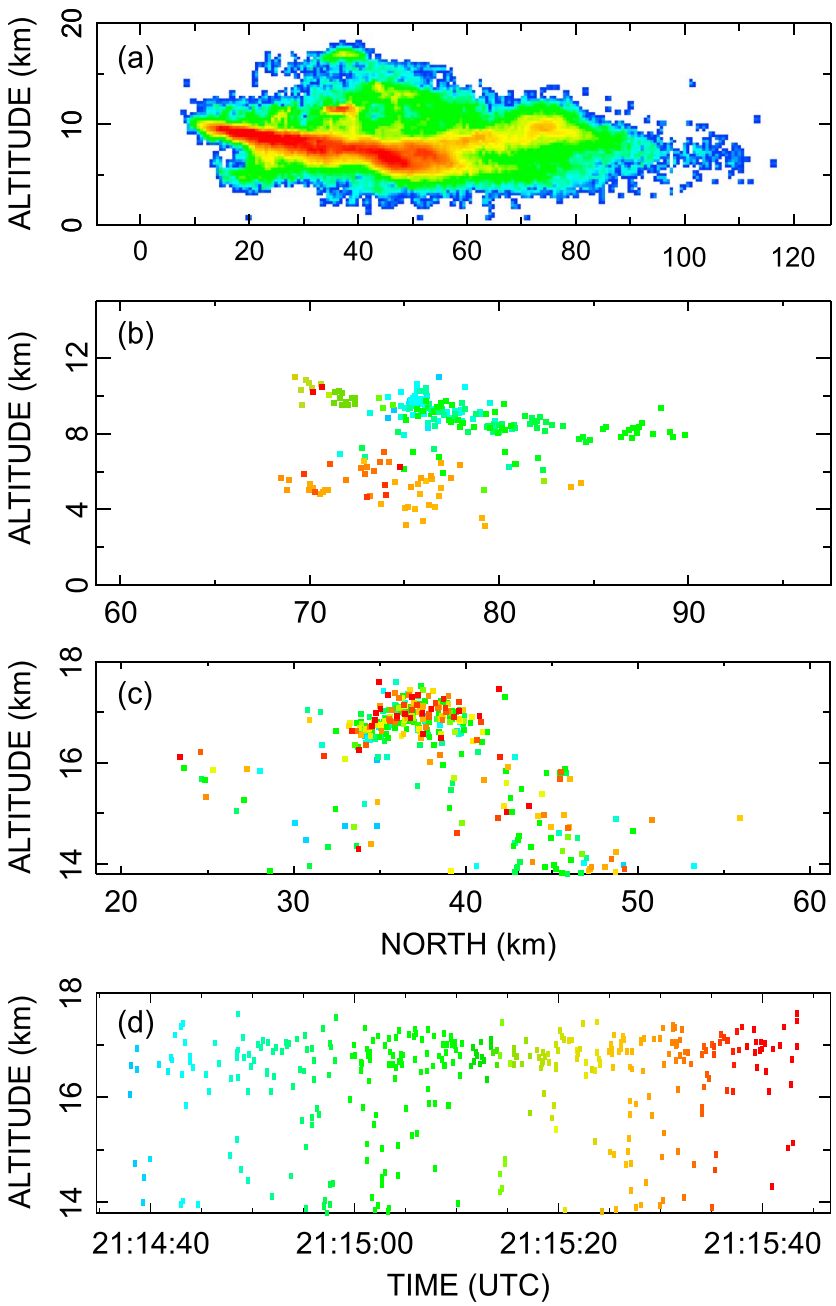

Figure 1. Examples of OK-LMA data at roughly 2115 UTC on 24 May 2011. (a) North versus altitude of VHF source density illustrating activity in an overshooting top during a 5.5 min period (2113:45–2119:16). The color scale indicates log density increasing from blue to red, automatically scaled to span the range of densities. Although density values are unknown, a total of 127,087 sources were included. (b) North versus altitude of VHF sources (262 total) from a typical bilevel cloud flash, lasting 1 s (2115:19.4–2115:20.4). (c) North versus altitude of 369 VHF sources that occurred above 14 km during approximately 1 min (2114:37–2115:43). (d) Time versus altitude of the same VHF sources as in panel c. Note the differences in horizontal and vertical scales in plots (Figures 1a–1c). Colors in plots Figures 1b–1d indicate the progression of time, varying smoothly from cyan to red spanning each period. The number of sources in the overshooting top peaked at roughly 17 km msl. In plots Figures 1a–1c, horizontal distance is measured from the center of the OK-LMA network.

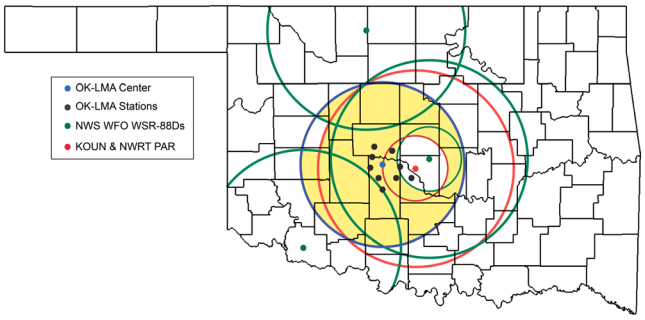

Figure 2. Map of the observational domain (yellow shading) for this study, with county boundaries, the center and one station of the OK-LMA network (blue dot), OK-LMA stations (black dots), KOUN and NWRT PAR 40 km and 120 km range rings (red circles), and NWS WSR-88Ds range rings (green circles). The blue circle shows the 100 km range ring centered on the OK-LMA. The yellow shaded observational domain is the overlap of the OK-LMA domain with the various radar domains.

systems sample overshooting tops continuously, while WSR-88D radar scans take 5–6 min and provide coarse resolution of storm height.

2. Instrumentation and Methodology

2.1. Lightning Mapping Data

Observations of total lightning were obtained from the Oklahoma Lightning Mapping Array (OK-LMA), which is located in west central Oklahoma [*MacGorman et al.*, 2008; *Barth et al.*, 2015] and contained 11 stations for storms during 2007–2009 and contained the 10 stations shown in Figure 2 in 2011 (a station near the Oklahoma City airport had been removed by 2011). The performance of Lightning Mapping Arrays is described by *Rison et al.* [1999], *Thomas et al.* [2004], and *Chmielewski and Bruning* [2016]. Each station of the OK-LMA detects up to one pulse every 80 μs (up to 12,500 s^{-1}). The time and location at which a VHF signal received by multiple stations was radiated is then calculated from the differences in times of arrival of the signal at the stations. To maintain good accuracy, particularly in the altitude of mapped sources, the VHF sources provided by the OK-LMA for this study were restricted to a range of ≤100 km from the center of the array. At that range, standard errors in the mapped sources are within 30 m in the horizontal, 200 m in the vertical, and 40 ns in time [*Thomas et al.*, 2004]. To provide greater reliability, VHF signals detected by fewer than eight stations or having computed time and location with reduced χ^2 values ≥2 were not used.

Flash rates for storms analyzed in this study were obtained by using the flash sorting algorithm in XLMA display software provided by New Mexico Institute of Mining and Technology [*Thomas et al.*, 2004]. Much as described by *MacGorman et al.* [2008], VHF sources were grouped together to create flashes based upon the elapsed time and distance between them. A new source was grouped with previous sources in a flash if it occurred within 150 ms of the last point already in the flash and occurred within 500 ms and 3 km horizontally and 5 km vertically of any point in the flash. To prevent flash durations longer than is usually observed, flash durations were limited to less than 3 s. (The record for flash duration observed by LMAs is >5 s [*Lang et al.*, 2017], but even 3 s flashes are rare. When observed, longer duration flashes typically have extended into the stratiform precipitation region of a mesoscale convective system.) A minimum of 10 VHF sources was required before a group of VHF sources meeting these criteria was included in our flash analyses. Flashes also were subdivided by number of VHF sources, which tends to increase with increasing channel length: large flashes had >75 sources; small to medium flashes had 10–75 sources.

Time-height source density plots were created to assess the evolving vertical structure of electrical activity through time. These were generated every 30 s and every 100 m of altitude by summing the number of sources in bins 60 s wide by 200 m of height centered on the nominal time and height. In our analysis, the LMA overshooting top signature is defined as ≥4 VHF sources per minute in a 200 m layer clustered above the LNB within a horizontal distance consistent with the size of overshooting tops (typically a few kilometers to roughly 10 km).

Percentiles of VHF source heights were calculated on 60 s of data every 30 s for the 50th (median), 90th, 99th, 99.73th, and the 99.99th percentiles. For convenience, the percentiles will hereafter be referred to as LMA_{50}, LMA_{90}, LMA_{99}, $LMA_{99.73}$, and $LMA_{99.99}$, respectively. When performing correlations with radar data, $LMA_{99.99}$ was selected because it represented the approximate maximum height of VHF sources while eliminating most lone outliers and errors. Additionally, a 5 min centered running average was imposed on the percentile data so that it was better aligned with the ~5 min timing of radar volume scans.

2.2. Radar Data

Most radar data used in this study were provided by the KOUN polarimetric research radar located in Norman, Oklahoma. This originally was the prototype radar for the S band (approximately 10 cm wavelength) Weather Surveillance Radar-1988 Doppler (WSR-88D) [*Crum and Alberty*, 1993] but was modified to provide polarimetric variables (differential reflectivity ZDR, correlation coefficient ρ_{hv}, and differential phase φ_{DP}), in addition to the conventional Doppler radar moments (radar reflectivity Z, radial velocity V_r, and spectrum width σ_v) [*Doviak et al*., 2000; *Ryzhkov et al*., 2005]. For most of the analyzed cases, the time required for a volume scan ranged between 5 and 6 min, depending on the volume coverage pattern being used. The exception to this was a case on 1 June 2008, when KOUN was operated in "supersector" mode from 0213 UTC until 0358 UTC [*Kumjian et al*., 2010]. This scanning strategy collected full sector volume scans every 72 s over an 80° sector and oversampled to create 0.5° azimuthal spacing or "super resolution" [*Brown et al*., 2002, 2005].

For one case, additional radar data were provided by the National Weather Radar Testbed Phased-Array Radar (NWRT PAR), located in Norman, Oklahoma. The NWRT PAR is an S band (9.4 cm wavelength), electrically steered phased-array radar system [*Zrnić et al*., 2007], which allows it to scan the volume of a 90° sector in $\leq$60 s. Data were collected using an adaptive scanning strategy [*Heinselman and Torres*, 2011] consisting of 19 elevation angles, ranging from 0.5° to 52.9°. Despite these advantages, the relatively large beam width (ranging from 1.6° at boresight to 2.3° at ±45° from boresight), when compared to traditional WSR-88D radars (~1°), often led to excessive nonuniform beam filling problems and to inflation of upper level reflectivity at long ranges.

Supplemental radar data were provided by the National Weather Service (NWS) WSR-88D [*Crum and Alberty*, 1993] radars located in Twin Lakes, Oklahoma (KTLX); Fredrick, Oklahoma (KFDR); and Vance Air Force Base, Oklahoma (KVNX). These radars had essentially the same operating characteristics as KOUN, except at the time of data collection they had not yet been modified to collect polarimetric variables. Level II data from these radars were obtained from the National Climatic Data Center (NCDC, has.ncdc.noaa.gov).

2.3. Satellite Data

The satellite data used in this study were acquired from the NCDC Comprehensive Large Array-Data Stewardship System (CLASS; http://www.class.noaa.gov). Raw data in its native format and resolution were collected for all cases from both GOES East (GOES 12 and GOES 13) and GOES West (GOES 11). The temporal resolution of the satellite data ranged between 5 and 30 min, depending on the scanning strategy being employed. At times, this resolution was increased by using data from both GOES East and GOES West, useful especially during the slower intervals of the routine full disk scan. At nadir, the spatial resolution of the satellite data in the visible (0.65 μm) and IR (10.7 μm) channels was 1 km and 4 km, respectively. However, over the domain of this study, spatial resolution in the 10.7 μm channel was roughly 5–6 km [*Dworak et al*., 2012].

2.4. Other Data Sources

Tornado and severe hail ($\geq$2.5 cm) reports for all cases were obtained from the Storm Events Database (www.ncdc.noaa.gov/stormevents) at the National Climatic Data Center. While NCDC carefully reviews these reports for accuracy before publication, we performed secondary quality control to remove any remaining errors. In particular, reports were superimposed on animations of reflectivity to isolate and retain only those associated with specific thunderstorm cells. Attempts were made to relate NCDC storm reports to specific overshooting tops spatially, but the storm reports lacked the necessary spatial and temporal precision. The only exception was a precise location for the 15.24 cm hailstone near Gotebo, Oklahoma, on 23 May 2011, obtained from the research group which measured it (S. Blair, personal communication, 2011).

Environmental soundings were obtained from the Iowa Environmental Mesonet/Iowa State University Department of Agronomy GEneral Meteorology PAcKage (GEMPAK) data archive (mesonet.agron.iastate.edu/archive/). Thermodynamic profiles were then plotted by using the Skew-T/Hodograph Analysis Research Program (NSHARP) [*Hart and Korotky*, 1991]. The available soundings were ill timed or poorly located for most of the storms we analyzed, so near the surface the sounding was modified by using surface data (e.g., temperature and mixing ratio) from the Oklahoma Mesonet [*Brock et al*., 1995]. Calculations of thermodynamic variables were based on the most unstable parcel, in order to provide the largest theoretical CAPE values.

Table 1. Date, Time of Observation (in UTC), and Storm Type for the Five Cases Presented in This Study[a]

Case	Date	Time of Observation	Storm Type	KOUN	NWRT PAR	NWS WSR-88Ds
1	24 May 2011	1900–2150	Supercell	Yes	Yes	Yes
2	23–24 May 2011	2030–0050	Supercell	Yes	No	Yes
3	1 June 2008	0100–0730	Supercell	Yes	No	Yes
4	7–8 September 2007	2230–0130	Multicell	Yes	No	Yes
5	23–24 April 2009	2300–0230	Multicell	No	No	Yes

[a]Also indicated are the availability of KOUN, NWRT PAR, and NWS WSR-88D data.

2.5. Data Synthesis

The Warning Decision Support System-Integrated Information (WDSS-II) [*Lakshmanan et al*., 2006, 2007] was used to synthesize, visualize, and analyze the diverse types of data. For radar data, we used WDSS-II to produce plan position indicator (PPI) and range-height indicator (RHI) plots and to calculate the maximum estimated size of hail (MESH) [*Ortega et al*., 2009] and the maximum height of various reflectivity levels (echo tops, ETs). To increase the accuracy of algorithms, Rapid Update Cycle (RUC) [*Benjamin et al*., 2004] analyses were ingested, when applicable, as described by *Lakshmanan et al*. [2006]. Additionally, plots of OK-LMA source points, source density, and contoured source density were superimposed on radar plots.

For our estimates of echo tops, radar data were interpolated between two elevation angles by using a bracketing technique described by *Lakshmanan et al*. [2013]. To minimize the impact of beam broadening with increasing range from the radar, analyses of echo tops and MESH were limited to a range of 120 km from any radar. To avoid errors caused by the radar "cone of silence," analyses were also restricted to ranges $\geq$40 km. At a height of 16 km above ground level from a WSR-88D radar within these range limits, the vertical separation of elevation scans is roughly 2–3 km for the Volume Coverage Pattern 11 (VCP 11) often used during NWS storm operations, and the WSR-88D beam width is 0.65–1.95 km.

Satellite overshooting top detections were determined manually in a process similar to the objective IR window-texture method of *Bedka et al*. [2010]. Here the presence of an OT was inferred by a cluster of IR pixels with brightness temperature less than the LNB temperature (derived from proximity soundings) and with horizontal dimensions consistent with OTs (typically a few kilometers to roughly 10 km). The analyses presented in this paper were based on the minimum temperatures in the overshooting top and did not depend, for example, on the associated gradients in temperature.

3. Storm Case Selection

An extensive search through the OK-LMA archive was performed to identify cases from 2004 to 2012 that met the following criteria (the union of criteria 2 and 3 composes the observational domain, Figure 2):

1. Continual LMA source points were present for some period in the overshooting top.
2. The storm remained $\leq$100 km from the OK-LMA network center for more than 95% of its lifetime.
3. The storm remained $\leq$120 km and $>$40 km from the radars being used for more than 95% of its lifetime.
4. The storm remained relatively isolated from other nearby convection.
5. Radar data were available for the storm (KOUN and NWRT PAR data being preferred).
6. Satellite data were available (preference given to rapid or super rapid scan operation).

While many cases met the first criterion, cases meeting all criteria were relatively rare. We selected five cases for analysis (Table 1) to provide a variety of convective modes and meteorological conditions. Table 2 summarizes the thermodynamic and dynamic parameters for each case.

The distribution of VHF sources relative to radar reflectivity is illustrated for contrasting storms, the supercell storm on 24 May 2011 (Figures 3a and 3c) and the multicell storm on 8 September 2007 (Figures 3b and 3d). Both show VHF sources above the LNB superimposed on a vertical cross section and a high-altitude constant elevation or constant altitude scan of radar reflectivity. In both cases, the VHF sources are distributed around and above an upward bulge of reflectivity indicative of an overshooting top. In the case of the supercell storm (Figures 3a and 3c), the sources also are above a bounded weak echo region.

Table 2. Thermodynamic and Dynamic Parameters for the Five Analyzed Cases[a]

	Case 1	Case 2	Case 3	Case 4	Case 5
	5-24-2011	5-23-11	6-1-08	9-8-07	4-24-09
Thermodynamic Parameter	1800	1800	0000	0000	0000
Most unstable parcel CAPE (J kg^{-1})	4287	4432	4325	2589	1946
Level of neutral buoyancy					
Height (km)	13.5	13.5	14.7	15.2	13
Temperature (°C)	−62	−63	−66	−73	−64
Maximum parcel level (km)	18	18	18.2	18	14.6
Maximum overshoot (km)	4.5	4.5	3.5	2.8	1.6
Temperature lapse rate (°C km^{-1})					
700–500 mb	8.2	9.4	8.4	6.9	8.8
850–500 mb	7	7.8	7.1	6.5	8.2
Magnitude of 0–6 km difference in horizontal wind vectors (m s^{-1})	17	16	22	15	11
0–3 km storm-relative helicity (m^2 s^{-2})	180	131	201	198	268
Environmental freezing level (km)	4.4	4.3	4.6	4.7	3.9
Updraft freezing level (km)	5.8	5.8	6	6	4.3
Tropopause height (km)	13.6	13.5	13.1	15.2	11.5

[a]Sounding data have been modified with Oklahoma mesonet data to account for surface conditions near convective initiation. Parcel trajectories are calculated assuming a most unstable parcel with virtual temperature correction. The time (UTC) and date are those of the premodified sounding.

4. Storm Overviews

4.1. Case 1: 24 May 2011

During the afternoon of 24 May 2011, a severe weather outbreak in central Oklahoma initiated several long-lived supercell thunderstorms along a well-defined dryline and produced hail with diameters ≥5 cm and 12 tornadoes. The cyclic supercell storm chosen for analysis produced an EF-3 tornado and an EF-5 tornado (Figure 4c). This storm began as a cluster of cells but intensified rapidly to become a supercell by 1922 UTC, with a clear hook echo and low-level velocity couplet (not shown). A debris ball in reflectivity suggested a tornado was inflicting surface damage from 2048 to 2146 UTC. Although the storm remained a tornadic supercell after 2146 UTC, the contamination of subsequent storm mergers complicated our analysis.

Lightning activity began shortly after 1900 UTC, as the cluster of storms began merging and strengthened (Figure 4d). Flash rates remained <30 min^{-1} for approximately 40 min. As the storm became a supercell, total flash rates increased rapidly, reaching 60 min^{-1} by 1950 UTC. After then remaining steady for roughly 15 min, flash rates surged again to 180 min^{-1} by 2012 UTC (the surge satisfied the objective 2 sigma lightning jump criteria of *Schultz et al.* [2011]) and continued increasing to a peak of 350 min^{-1} at 2037 UTC. Flash rates then declined to 250 min^{-1} over the next 30 min. Another lightning jump occurred at 2110 UTC, as flash rate increased to 430 min^{-1}. Although one large hail report preceded the first lightning jump, subsequent severe weather reports, including tornado reports, followed large increases in flash rates, similar to the trend found by several investigators [e.g., *Williams et al.*, 1999; *Schultz et al.*, 2011; *Chronis et al.*, 2015].

This is the only storm in this study that had a sudden large decrease in VHF source rates and in rates of large flashes in the middle of a period of huge total flash rates (at approximately 2110 UTC). We have been unable to find a corresponding change in operating characteristics of the OK-LMA that could cause this behavior. Because this behavior of flashes is immaterial to our conclusions, however, this study did not examine whether there were corresponding changes in other storm properties that might have caused the change in these rates.

4.2. Case 2: 23–24 May 2011

On 23–24 May 2011, the day before Case 1, long-lived supercell storms developed along a well-defined dryline in west central Oklahoma and produced large hail and two EF-0 tornadoes. The storm chosen for analysis produced no tornadoes but did produce hail, including a hailstone 15.24 cm in diameter

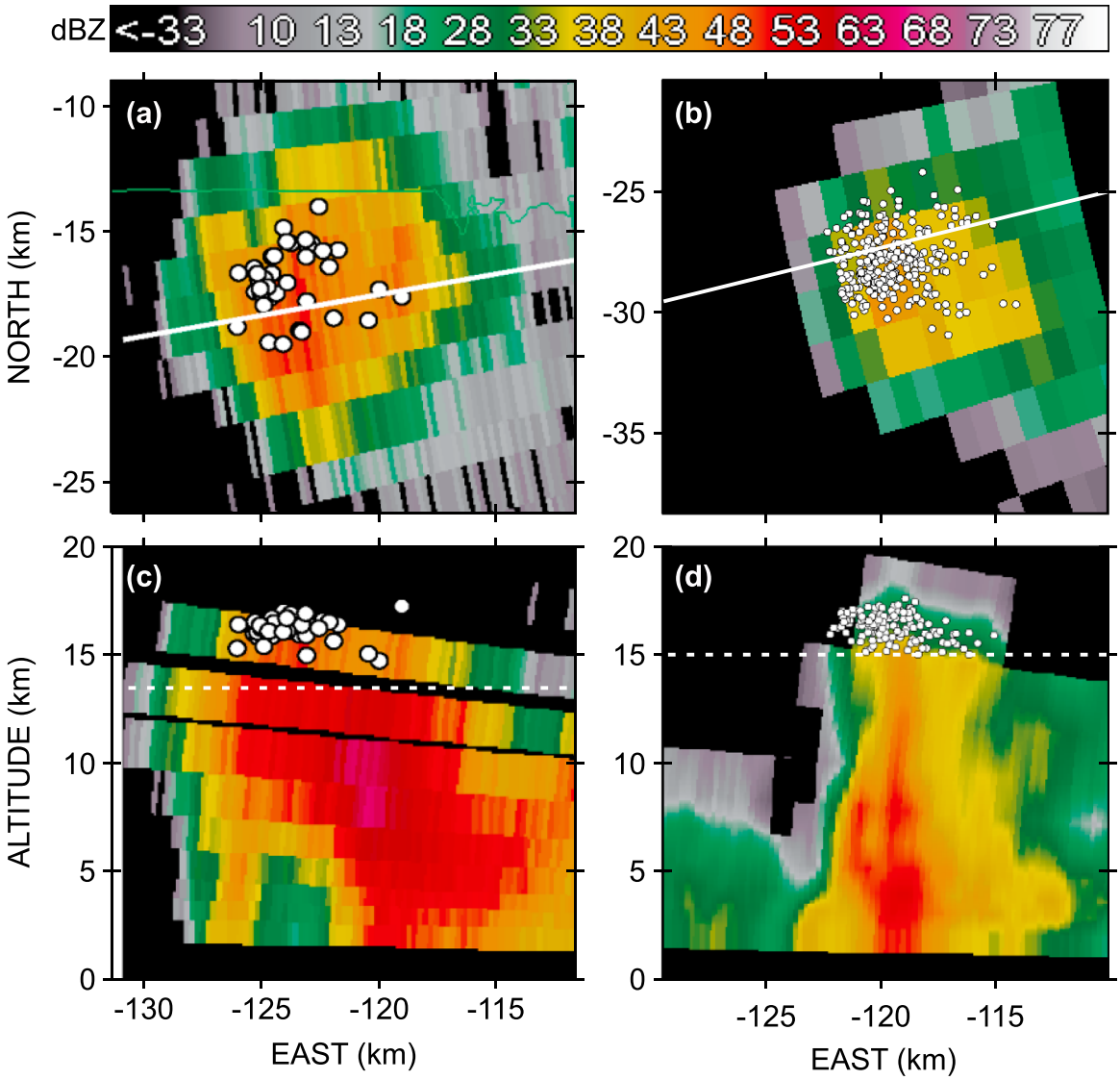

Figure 3. VHF sources above the LNB (dashed line) superimposed on radar reflectivity. (a, c) 24 May 2011 supercell. Radar data at 1954:45 UTC from the NWRT PAR with VHF sources from 1 min centered on the time of the radar scan. Reflectivity from the 6.4° elevation angle (Figure 3a). Altitude varies from 14 km msl on the right edge to 16 km MSL on the left edge. All VHF sources above the LNB superimposed on the vertical cross section along the radial (white line) in Figure 3a (Figure 3c). (b, d) 8 September 2007 multicell. VHF sources are from the 5 min period of the volume scan by the KOUN radar. Constant altitude plot of radar data at an altitude of 13.5 km msl (Figure 3b). Superimposed VHF sources are within 1 km of the vertical cross section of radar reflectivity along the radial (white line) in Figure 3b (Figure 3d).

(Figure 5c), a record for Oklahoma (records maintained since 1950). After beginning in a cluster of cells, the storm took less than 30 min to form a well-defined supercell structure. For 3 h it maintained a hook echo and a relatively weak low-level velocity couplet and then dissipated rapidly (both visually and in radar data) over a 30 min period.

Electrical activity in the 23–24 May 2011 storm began at 2036:30 UTC (Figure 5d), 14 min after the first radar echo. For more than an hour, total flash rates remained $\leq 30\,\mathrm{min}^{-1}$. Shortly after 2200 UTC, however, total flash rates increased rapidly to more than $125\,\mathrm{min}^{-1}$ in less than 20 min and satisfied the 2 sigma criteria for a lightning jump [*Schultz et al.*, 2011]. After remaining relatively constant for roughly 10 min, flash rates again increased rapidly to $180\,\mathrm{min}^{-1}$ at 2247:30 UTC, their maximum value for the storm. Flash rates remained large ($>125\,\mathrm{min}^{-1}$) until roughly 2330 UTC, after which they steadily declined.

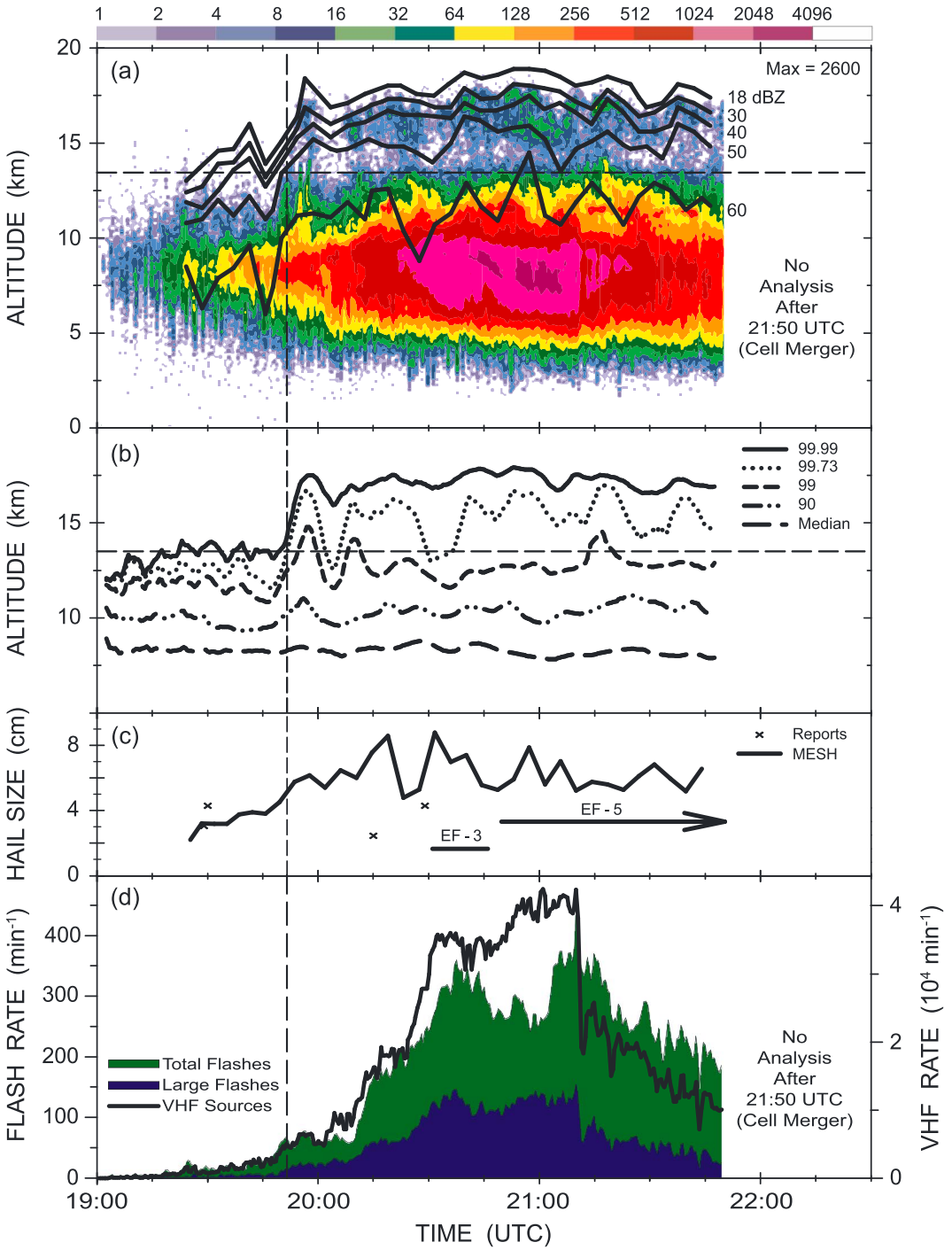

Figure 4. Evolution of lightning relative to radar reflectivity and severe weather reports in a supercell storm on 24 May 2011. The horizontal dashed line in plots showing height depicts the LNB inferred from an environmental sounding. The vertical dashed line in this plot denotes the onset of the VHF overshooting top signature. In other plots, vertical dashed lines denote the onset and end of the VHF overshooting top signature. (a) Time-height plot of VHF source density (color shading; in units of number of sources per 200 m per min) and of radar-estimated echo top (solid black lines) for various radar reflectivity values. (b) Percentiles of the height of VHF sources, indicating the percentage of sources at altitudes lower than the plotted altitude. (c) Severe weather reports for hail and tornadoes. Reported hail size is indicated by a cross. Each horizontal line indicates the time of a tornado, labeled with its EF damage rating. The solid line indicates the maximum hail size estimated from radar data (MESH). (d) VHF source rates (solid line), total flash rates (green shading), and rates of flashes having >75 VHF sources (blue shading).

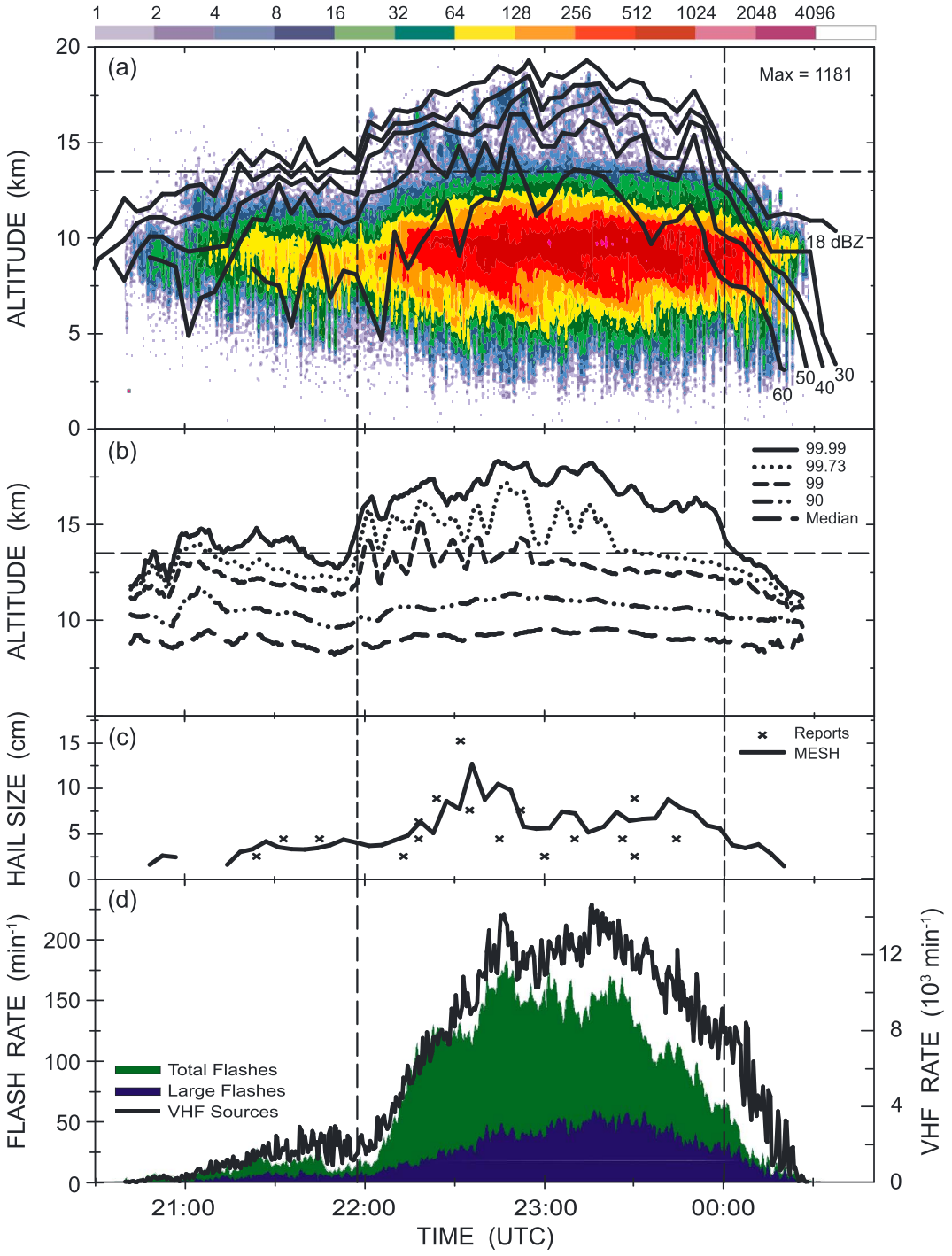

Figure 5. Evolution of lightning relative to radar reflectivity and severe weather reports in a nontornadic supercell storm on 23–24 May 2011. (See caption for Figure 4.)

4.3. Case 3: 1 June 2008

Shortly after 0000 UTC on 1 June 2008, convective storms began developing in western Oklahoma along a stalled frontal boundary [*Kumjian et al.*, 2010]. Over the next 7 h, two supercell storms formed, producing many reports of severe hail (≥2.54 cm in diameter), but no tornadoes. The first echo for the analyzed storm occurred at 0111 UTC (Figure 6a). After quickly developing supercell characteristics, the storm split, with the weakening left mover traveling northeastward and the dominant supercell traveling southeastward. By

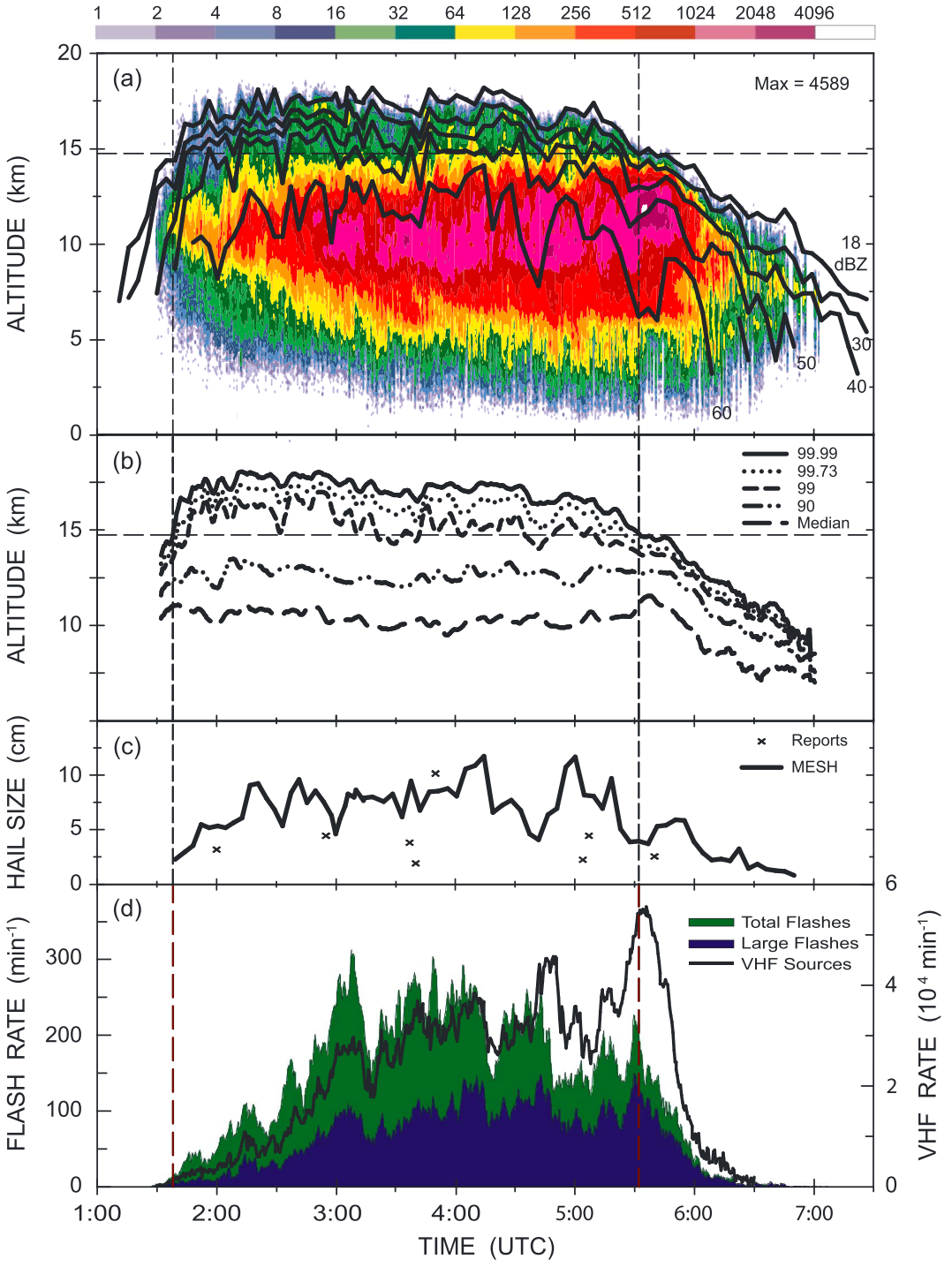

Figure 6. Evolution of lightning relative to radar reflectivity and severe weather reports in a nontornadic supercell storm on 1 June 2008. (See caption for Figure 4.)

0300 UTC, a second supercell storm had developed along the rear flank of the dominant supercell and continued strengthening over the next hour. By 0430 UTC, the supercell storms had merged into a massive cluster, which maintained a well-defined hook echo for more than an hour. The storm then began weakening and dissipated completely soon after 0700 UTC.

The first lightning flash (0120 UTC) in the 1 June 2008 supercell began <10 min after the first radar echo. Total flash rates (Figure 6d) increased rapidly, with lightning jumps occurring at 0142, 0153, 0228, and

0245 UTC. After the 0245 UTC lightning jump, total flash rates peaked at 313 min^{-1}. This was soon followed by a series of oscillations as the total flash rate fluctuated between 150 and 300 min^{-1}. Severe hail reports and the larger increases in estimated maximum hail diameter from MESH (Figure 6c) both tended to follow lightning jumps.

4.4. Case 4: 7–8 September 2007

At 2233 UTC on 7 September 2007, a multicell storm began in southwest Oklahoma along a residual outflow boundary from earlier convection, and cells propagated north-northeastward. As cells intensified, weakened, and produced outflow boundaries, new cells developed along the new boundaries and repeated the cycle. One cell developed on the southern flank of the cluster around 0018 UTC and moved eastward as it tracked along the original outflow boundary. This cell persisted longer (roughly 60 min) and was much stronger than the transient (~20 min duration) cells that moved north-northeastward. Although a severe thunderstorm warning was issued for this cell, no severe weather was reported before the storm dissipated completely shortly after 0147 UTC.

The storm's first lightning flash occurred at 2312:30 UTC, 40 min after the first radar echo. Initially, total flash rates (Figure 7d) in cell A remained $< 5\ min^{-1}$, and almost all flashes had >75 VHF sources each. A new cell (cell B) developed shortly before 0000 UTC, and its total flash rate increased steadily, peaking slightly above 20 min^{-1} at 0008 UTC. After 0018 UTC, total flash rates from cell B fell rapidly as the cell weakened, and a new, more vigorous cell (cell C, the eastward moving cell) began developing. Cell C had a larger lightning jump than cell B, with total flash rates increasing from 3 min^{-1} to a peak of 41 min^{-1} over a 12 min period. As in previous cases, the lightning jump correlated well with a sudden increase in the rates of medium-size flashes (Figure 7d), with rates of large flashes having far less influence on total rates. Total flash rates subsequently fluctuated between 15 and 30 min^{-1}, before beginning to decline sharply at 0102 UTC as the storm dissipated. The last flash was observed at 0118 UTC.

4.5. Case 5: 23–24 April 2009

This case formed as a region of weakening convection moved into greater moisture in southwestern Oklahoma and storms began redeveloping, with the first echo of a storm in this redevelopment occurring at 2318 UTC on 23 April 2009. By 2344 UTC, the redeveloping storm had become a multicell which gradually strengthened as it propagated northeastward toward central Oklahoma over the next hour. The height of reflectivities ≥40 dB*Z* reached a peak shortly before 0050 UTC and then decreased fairly steadily over the next hour as the storm dissipated. Although a severe thunderstorm warning was issued for much of this storm's lifetime, the only hazard report was for a hail size that is no longer considered severe and occurred as the maximum height of 50 dB*Z* decreased rapidly as the storm dissipated.

The first lightning flash from the redeveloping storm occurred at 2322 UTC (Figure 8d), only 4 min after the first radar echo was observed. Initially, total flash rates increased to 50 min^{-1} over a 20 min period and then fluctuated between 40 and 80 min^{-1} over the next hour. An increase in discharges in the overshooting top (pulse 1 in Figure 8a) began at 0002 UTC, just before a local maximum in total flash rates of 60 min^{-1}. At 0029 UTC, a dramatic lightning jump occurred, with total flash rates increasing from 75 to a peak of 211 min^{-1} over a 9 min period (Figure 8d) during which the height of discharges in the overshooting top increased to its fourth peak (Figure 8a). Flash rates fluctuated above 200 min^{-1} until reaching a peak of 238 min^{-1} at approximately 0050 UTC and then began to decline. After 0105 UTC, flash rates fell rapidly from 150 min^{-1} to $<10\ min^{-1}$ by 0120 UTC and remained low until the last flash occurred approximately 30 min later.

4.6. Trends in Flash Sizes and VHF Source Rates

VHF source rates tended to reflect variations in flash rates for large flashes (>75 VHF sources per flash) better than for total flashes, with peaks in VHF sources typically reflected by corresponding peaks in rates of large flashes (Figures 4d, 5d, 6d, 7d, and 8d). Similarly, large increases in total flash rates (such as those satisfying the "lightning jump" criteria) often did not align with large increases in rates of large flashes and in rates of VHF sources but tended to align much better with increases in rates of small to medium flashes (10–75 VHF sources per flash). This is consistent with the observation by *Schultz et al*. [2015] that mean flash sizes tended to be smaller during relatively large increases in total flash rates as storms intensified and to be larger when updrafts were weakening.

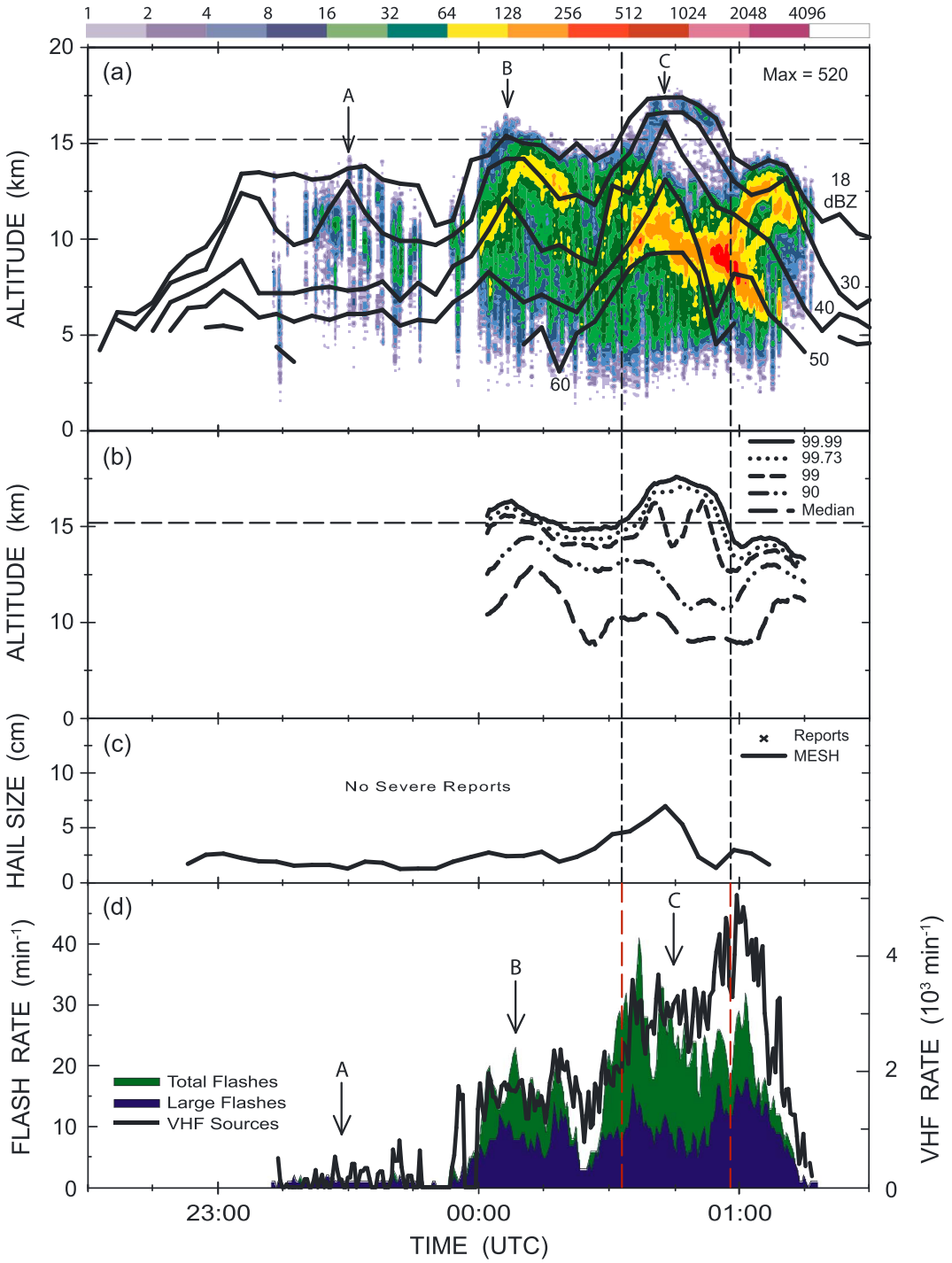

Figure 7. Evolution of lightning relative to radar reflectivity and severe weather in a multicell storm on 7–8 September 2007. (See caption for Figure 4.)

Initially, rates of both VHF sources and large flashes tended to increase in response to the increasing intensity and size of the storm. However, a decrease in both rates did not necessarily mean the storm's potential for severe weather was decreasing, as a tornado rated EF-5 continued on the ground at least several tens of minutes after a sudden decrease in both at approximately 2110 UTC on 24 May 2011 (Case 1), and the radar-estimated hail size remained severe after rates in both began decreasing on 23–24 May 2011 (Case 2). Furthermore, VHF source rates could increase without the potential for severe weather increasing. One

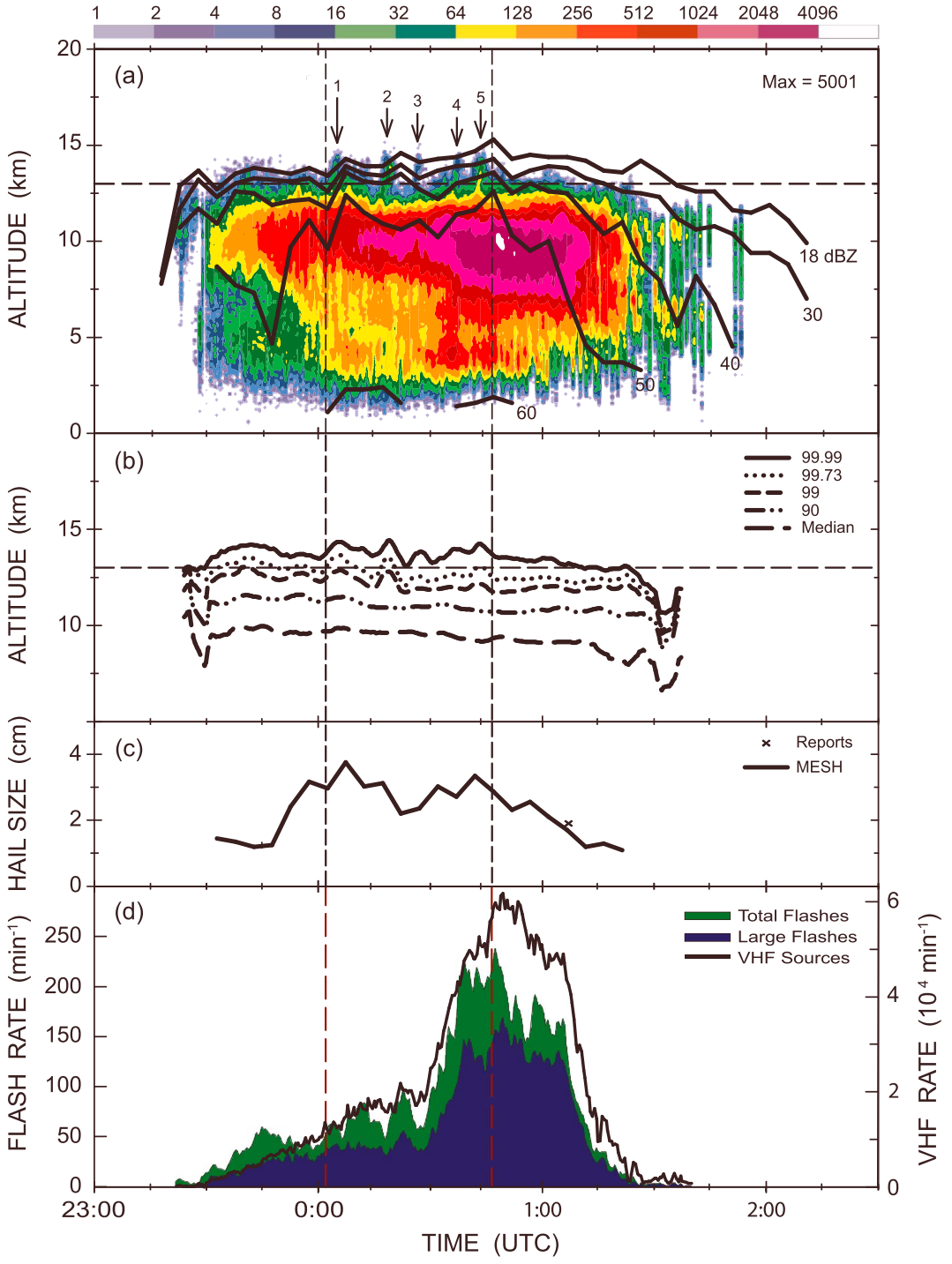

Figure 8. Evolution of lightning relative to radar reflectivity and severe weather in a multicell storm on 23–24 April 2009. (See caption for Figure 4.)

could argue that the most reliable signature of storm evolution provided by VHF source rates and rates of large flashes was for storm dissipation. In three of the four storms observed during dissipation, VHF source rates rapidly increased to their maximum value as the storm began dissipating (Figures 6–8). In all four storms (Figures 5–8), the fraction of flashes composed of large flashes increased as the storms dissipated, similar to the finding by *Bruning and MacGorman* [2013] that flash size tended to be larger in regions in which flow was more laminar, away from strong updrafts.

5. Discharges in the Overshooting Top

To examine the timing of discharges in the overshooting top (OT) relative to storm evolution, a primary goal of this study, we plotted the time history of the vertical distribution of VHF sources relative to flash rates, severe weather reports, and the maximum height of various reflectivity values.

5.1. Case 1: 24 May 2011

Initially (1900–1950 UTC), on 24 May 2011, vertical source densities $\geq$4 sources per 200 m of altitude per min were mostly confined between 4 and 12 km (Figure 4a), the largest source densities being between 6.5 and 9.5 km and remaining $<$512 (200 m)$^{-1}$ min^{-1}. A rapid rise in the altitude of source densities (termed a "lightning bubble" by *Ushio et al.* [2003]) began shortly before 1950 UTC, with source densities between 16 and 32 (200 m)$^{-1}$ min^{-1} surging from 11 km to near the LNB at 13.5 km. At 1951:35 UTC, VHF source densities $<$4 (200 m)$^{-1}$ min^{-1} continued surging above the LNB to start the VHF OT signature. The upward pulse in $LMA_{99.99}$ (Figure 4b) reached an altitude of 17.4 km by 1954:50 UTC before leveling off. Thus, the initial pulse of $LMA_{99.99}$ was associated with an average rise rate of 20 m s^{-1} while above the LNB, but vertical source densities above the LNB remained rather meager ($<$8 (200 m)$^{-1}$ min^{-1}).

Between 2000 UTC and 2007 UTC, there was a lull to $<$ 4 (200 m)$^{-1}$ min^{-1} in vertical source densities. This lull was short lived. By 2007 UTC, regions with densities $\geq$4 (200 m)$^{-1}$ min^{-1} appeared abruptly at altitudes between 14.5 and 17 km (Figure 4a), the sudden appearance contrasting with the continual rise from below the LNB during the initial penetration.

Throughout the remainder of the analysis period, a quasi-steady VHF OT signature persisted. Overall, vertical source densities above the LNB were greatest (e.g., 8–64 (200 m)$^{-1}$ min^{-1}) between 15 and 18 km and smallest between 13.5 and 15 km. Vertical source densities in the upper region appeared cyclic, with increases typically appearing suddenly at altitude, rather than rising from below. The maximum densities (e.g., 64–128 (200 m)$^{-1}$ min^{-1}) above the LNB were at 2114–2122 UTC between 16.5 and 17.5 km and began 4 min after the storm's maximum flash rate. The height of $LMA_{99.99}$ also oscillated, reaching an apex of 17.8 km at 2051 UTC and cresting at successively lower altitudes thereafter (Figure 4b).

The onset of the VHF OT signature appeared to be an indicator of the storm's potential for producing increasingly severe hazards, as it occurred approximately 14 min before the first tornado warning (not shown) and 37 min before the first tornado was reported (Figures 4a and 4c). Note that the onset of the VHF OT signature preceded the lightning jump (at 2007 UTC, mentioned previously) by at least 15 min. While a few severe hail reports were received about 20 min before the onset of the VHF OT signature, the radar-based hail estimate (MESH) was greatest while the VHF OT signature was present. Although no hail reports were received after 2030 UTC, it is possible that spotter attention was focused entirely on the EF-3 and EF-5 tornadoes tracking through the Oklahoma City metropolitan area, not on hail.

5.2. Case 2: 23–24 May 2011

Throughout the initial stages of electrical development (2040–2157 UTC), vertical source densities $\geq$4 (200 m)$^{-1}$ min^{-1} were typically between 4 and 12 km, the greatest densities ($\geq$64 sources min^{-1}) being between 7 and 10 km (Figure 5a). The onset of the VHF OT signature began at 2157:30 UTC, as a lightning bubble began rising from just below the LNB and reached an altitude of 16.8 km by 2202:30 UTC, an average rise rate of 11 m s^{-1} (compare with an initial rise rate of 20 m s^{-1} in Case 1). Vertical source densities above the LNB remained small ($<$8 sources min^{-1}) throughout the lifetime of this bubble.

VHF sources above the LNB ceased temporarily (i.e., 2203–2207 UTC) immediately after the initial lightning bubble, reappeared shortly thereafter, and continued cyclically until 0000 UTC, when the VHF OT signature finally ended, approximately 2 h later. After the signature dissipated, the maximum height of VHF source densities $\geq$4 (200 m)$^{-1}$ min^{-1} fell, and lightning completely dissipated within 30 min.

While the VHF OT signature was present, the height of $LMA_{99.99}$ (Figure 5b) oscillated, a pattern similar to what was observed in Case 1. Successive crests of $LMA_{99.99}$ increased until reaching an apex of 18.2 km at 2243 UTC, remained above 18 km until ~2314 UTC, and then decreased until $LMA_{99.99}$ fell below the LNB at ~0010 UTC. Maximum vertical source densities above the LNB also were cyclic, with maxima increasing to

16–32 sources min^{-1} by 2252 UTC (Figure 5a). Much as in Case 1, vertical source densities above the LNB during much of the OT signature had minima below 15 km and a maxima between 15 and 18 km.

The onset of the VHF OT signature again preceded an increase in the severity of the hazards produced by the storm (Figures 5a and 5c). For example, while a few hail reports were noted as much as 35 min before the onset of the VHF OT signature, the majority (including the 15.24 cm record hailstone and all hail reports $\geq$ 5.04 cm) occurred while the VHF OT signature was present. Radar-inferred hail size (MESH) was also greatest during this period. Finally, the delay in the lightning jump was shorter than in Case 1, being only 5 min after the onset of the VHF OT signature.

5.3. Case 3: 1 June 2008

Initial VHF source densities increased much more rapidly and tended to occur somewhat higher in altitude in Case 3 than in Cases 1 and 2, although they all were supercell storms (Figures 4a, 5a, and 6a). On 1 June 2008, the maximum height of sources increased rapidly, penetrating the LNB (which also was higher than in the first two cases) to begin the VHF OT signature at 0038 UTC, approximately 18 min after the first flash. Although not as obvious as in the previous cases, the initial penetration of VHF sources above the LNB was again associated with a lightning bubble rising from below. $LMA_{99.99}$ (Figure 6b) rose from the LNB to an altitude of 16.7 km in about 4 min, a rise rate of approximately 8 m s^{-1}.

After the initial penetration, $LMA_{99.99}$ oscillated between 16.5 and 17 .5 km, before reaching an apex of 17.9 km at 0210:30 UTC, approximately 30 min after initially rising above the LNB. Although not discernible at the time resolution in Figure 6a, the apex was associated with a lightning bubble originating at about 11.5 km roughly 4 min earlier, with a rise rate above the LMB of approximately 17 m s^{-1}. After this peak, cycles in the altitude of $LMA_{99.99}$ and in the maximum vertical source density continued for more than 3 h. Until 0456 UTC, the altitude of $LMA_{99.99}$ typically varied only hundreds of meters, with most peaks $>$17 km. Afterward, it declined fairly steadily until the LMA overshooting top signature ended at 0532 UTC. Between 0236 UTC and 0532 UTC, the nature of the peaks tended to alternate, with a rising bubble (peaking, for example, at around 0236, 0343, 0405, 0423, and 0450 UTC) typically followed by vertical source densities suddenly appearing in the upper part the overshooting top 5–10 min later (e.g., 0248, 0337, 0414, 0428, and 0456 UTC). Note that the VHF OT signature ended in the first supercell storm (A) at approximately 0343 UTC, and the peak at that time reflected the contribution from the adjoining strengthening supercell storm (B) which had begun its VHF OT signature.

On 1 June 2008, the maximum vertical source densities in the overshooting top tended to be larger than in Cases 1 and 2. The larger values typically occurred in the upper part of the overshooting top of storm A, which produced a maximum greater than 64 $(200\ m)^{-1}\ min^{-1}$ at times between 0250 UTC and 0305 UTC. Storm B had even larger maxima, reaching $>$128 $(200\ m)^{-1}\ min^{-1}$ shortly after 0400 UTC, but it differed from the other supercell storms in that the maxima were often in the lower part of the overshooting top rather than in the upper part.

As in the other cases, the onset of the VHF OT signature was associated with an increase in the severity of storm hazards (Figure 6c). In this case, the onset of severe values of estimated maximum hail size from MESH occurred about 5 min after the first appearance of the VHF OT signature. The first hail report (3.175 cm) was received 20 min after the onset of the VHF OT signature. However, no obvious patterns emerged in the timing of $LMA_{99.99}$ peaks relative to either severe reports or MESH. The first lightning jump (described in section 4.3) occurred only 3 min after the onset of the VHF OT signature, so both the lightning jump and the onset of the VHF OT signature provided similar lead times for hail reports and MESH hail estimates.

5.4. Case 4: 7–8 September 2007

This multicell storm intensified more slowly than all the other cases. Furthermore, its maximum flash rate was the smallest of all the cases (Figure 7d).

The first cell (cell A) failed to reach the LNB and took 40 min to produce its first flash. Although every flash in this cell had $>$75 VHF sources, flash rates never exceeded a few per minute, and both VHF source rates and maximum vertical source densities were relatively small (respectively $<$1000 min^{-1} and $<$64 $(200\ m)^{-1}\ min^{-1}$) (Figures 7a and 7d).

Cell B, on the other hand, grew more rapidly, and its 18 dB*Z* echo top briefly touched the LNB. Lightning was produced throughout much of its life, but the cell was relatively short lived. Maximum flash rates and maximum vertical source densities both were nearly an order of magnitude larger than in Cell 1. The maximum altitude of VHF sources and of vertical source densities >64 (200 m)$^{-1}$ min^{-1} both rose roughly 4 km in 10 min, at a rise rate of 16 m s^{-1}, and then fell. Although $LMA_{99.99}$ (Figure 7b) peaked briefly above the LNB, the VHF sources above the LNB were not clustered within a horizontal distance typical of on overshooting top (not shown), so it was not considered a VHF OT signature.

Cell C was the strongest cell in this storm; its 18 dB*Z* echo top and $LMA_{99.99}$ grew to roughly 2.5 km above the LNB (compared with 3–5 km overshoots in the supercell cases). Maximum vertical source densities and flash rates were both almost a factor of 2 greater than in Cell B. A lightning bubble was observed below the LNB just prior to the onset of the VHF OT signature. However, unlike the lightning bubbles in previous cases, its rise rate slowed considerably, to 3.2 m s^{-1}, as it approached the LNB, so $LMA_{99.99}$ took nearly 12 min to rise from the LNB to its apex of roughly 17.5 km. $LMA_{99.99}$ had a single ascent and descent, and the period of the VHF OT signature was a relatively short 25 min, reflected also in the cycle of 18–40 dB*Z* echo tops.

As in the other cases, the onset of the VHF OT signature again preceded an increase in the severity of the radar-inferred hazards associated with the storm (Figure 7c). The storm had no severe reports, and throughout the lifetime of both cells A and B, MESH remained at or below severe hail limits. However, as cell C strengthened, the hail size estimates from MESH began to increase and approached a diameter of 4.4 cm when the VHF OT signature first appeared. (The lack of actual hail reports during the 20 min MESH indicated severe hail could have been due either to overestimates by MESH or to the scarcity of observers as the storm traveled through a rural region.) Thus, the VHF OT signature lagged the onset of severe in MESH by roughly 6 min. The rise to a peak in estimated maximum diameter of ~7 cm and the subsequent drop in estimated diameter to below severe levels corresponded reasonably well with the growth and collapse of $LMA_{99.99}$. The timing of the lightning jump (described in section 4.4) agreed better with the onset of severe hail from MESH, lagging MESH by only ~1 min versus a lag of 6 min from the VHF OT signature.

5.5. Case 5: 23–24 April 2009

Although the VHF OT signature lasted longer in this storm than in the other multicell case (45 min versus 28 min), the distance $LMA_{99.99}$ penetrated above the LNB was the smallest of all the cases (a little more than 1 km versus $\geq$2.5 km) (Figures 4b, 5b, 6b, 7b, and 8b). However, its maximum flash rate was 5 times the maximum flash rate of the other multicell case, and its maximum vertical source density was 4 times that of the other case (Figures 7a, 7d, 8a, and 8d).

The initial surge of sources above the LNB (labeled pulse 1 in Figure 8a) to start the VHF OT signature began at approximately 0000 UTC and was associated with a lightning bubble rising from below to 14.3 km at 8.7 m s^{-1}. Although vertical source densities exceeding 4 (200 m)$^{-1}$ min^{-1} and $LMA_{99.99}$ (Figures 8a and 8b) were observed above the LNB well before the start of the VHF OT signature at 0002 UTC, closer examination of earlier periods found that the VHF sources were dispersed too far horizontally to fit within a traditional OT. VHF sources associated with pulse 1 above the LNB ceased after 12 min, followed by a relative minimum in $LMA_{99.99}$ and in vertical source densities of the OT that lasted until pulse 2 began.

Unlike the VHF OT signature for the other multicell storm (Case 4), which consisted of one rising and falling pulse of VHF sources, the VHF OT signature in Case 5 consisted of five discrete pulses of VHF sources rising above the LNB. After the first pulse, subsequent pulses above the LNB reached peak altitudes of 14.5, 13.8, 13.9, and 14.2 km; lasted 8, 3, 5, and 7 min; and rose above the LNB at 12.5, 6.7, 7.8, and 9.8 m s^{-1}. Note that the durations are much smaller than in Case 4. As in two of the other three cases analyzed during their dissipating stage, the largest value of vertical source densities in the entire storm and the largest VHF source rates occurred as the VHF OT signature ended and the storm began dissipating (Figures 6a, 6d, 7a, 7d, 8a, and 8d).

While hail diameter estimates from MESH began increasing nearly 15 min before the onset of the VHF OT signature (Figure 8c), it surpassed the severe threshold (2.5 cm) only 4 min before the beginning of the VHF OT signature. Additionally, the maximum MESH value of 3.8 cm was not observed until 5 min after the VHF OT signature was first detected. Thus, the timing of the onset of the VHF OT signature agreed reasonably well with the timing of the onset of severe MESH values. Despite MESH values being greater than the severe

threshold for most of the period of the VHF OT signature, there were no hail reports then. The only hail report, for a diameter no longer considered severe, was during the dissipation of the storm, well after the VHF OT signature. It is possible that the small hail core produced larger hail that went undetected as it traversed a rural area. The lightning jump (described in section 4.5) occurred nearly 30 min after the onset of the VHF OT signature and more than 30 min after MESH values reached severe levels. Thus, the onset of the VHF OT signature was a better predictor of increasing potential for severe weather than the lightning jump in this case.

6. VHF Overshooting Tops Relative to Radar and Satellite Observations

6.1. The LMA Overshooting Top Signature Relative to Radar Structure

Having data available from the NWRT PAR for the 24 May 2011 case provides an opportunity to examine the onset of the VHF OT relative to the reflectivity structure of the storm with approximately 1 min time resolution. By 1950:27 UTC (not shown), a reflectivity core near −122.5 km east, −24.5 km north (relative to the radar) had penetrated a height of 15 km but failed to produce VHF sources in the overshooting top. This reflectivity core of the storm rapidly weakened and completely dissipated by 1952:48 UTC. It was unable to sustain itself and lasted only 6 min (not shown). Maximum reflectivity above the LNB during this updraft pulse remained $<$ 40 dB*Z*.

A second more sustained penetration above the LNB was first visible as a 35 dB*Z* echo on the 6.4° PPI reflectivity scans at 1951:48 UTC, roughly 6 km northwest of the dissipating previous core (Figures 9a and 9d). Both the reflectivity value and the width of the new core increased rapidly, as its reflectivity above the LNB exceeded 50 dB*Z* within 2 min (Figures 9b and 9e). The first VHF sources in the VHF OT signature appeared as the reflectivity above the LNB increased to approximately 45 dB*Z* at 1952:48 UTC (not shown). The majority of these 13 sources were found near the outer edges of the reflectivity core at altitudes between 13.5 and 14.5 km.

Over the next 3 min (1952:48–1955:40 UTC), the area with reflectivity ≥45 dB*Z* and the area with ≥50 dB*Z* in the OT both expanded in size, and there was a large region of Z ≥ 65 dB*Z* at heights between 5 and 12 km, just above and downshear of a bounded weak echo region (BWER) (−125 to −122 km east; Figures 9b and 9e). The BWER and the region with ≥65 dB*Z* were both likely the product of a strong updraft, which suspended mixed-phase hydrometeors aloft long enough to allow particles of sufficient mass to form and fall out on the downshear side, near the edge of the main updraft. Throughout this period, the rate and height of the VHF sources emitted in the OT also increased, reaching a total of more than 60 min^{-1} and a height exceeding 17 km. The appearance of VHF sources in the OT morphed into a dome-like structure, with its apex at -122 km east, centered above the core reflectivity of the OT (Figure 9f).

By 2000 UTC, the maximum altitude of the heavy precipitation just downshear of the BWER had begun descending, and the rate of VHF sources in the OT had decreased (Figures 9g and 9j), although the area of ≥45 dB*Z* above the LNB remained large. The reflectivity values and the number of VHF sources in the overshooting top decreased rapidly over the next 4 min (Figures 9g and 9j, and 9i and 9l). During the decrease in VHF source rates in the OT, the VHF sources still tended to cluster near the larger OT reflectivities, and their maximum height also decreased. By 2004 UTC, the overshooting top had a maximum reflectivity $<$40 dB*Z* above the LNB and produced no more VHF sources (Figures 9i and 9l).

6.2. Evolution of Lightning Height Relative to Radar Echo Top Heights

Figures 4a, 5a, 6a, 7a, and 8a show how the timing of the vertical growth of storms depicted by VHF sources compares with the timing of vertical growth in the maximum height of 18, 30, 40, 50, and 60 dB*Z* reflectivity values in KOUN or WSR-88D data for the five analyzed cases. A visual inspection shows that the height of 18 and 30 dB*Z* echo tops typically was at or above the height of VHF source densities ≥ 4 (200 m)$^{-1}$ min^{-1}, and as would be expected from a common dependence on updraft cycles, variations in these echo tops were similar to variations in these VHF source densities, although there were some differences. Figures 4b, 5b, 6b, 7b, and 8b show the height of the median and of various large percentiles of the height of VHF sources for comparison with the echo tops. Note that the similarity in altitude between echo tops and VHF percentiles often worsens for larger reflectivities or for smaller percentiles. For the supercell cases, the median and 90th percentile are relatively constant, at least until the storm begins to dissipate, and so have little relationship with variations in the other parameters.

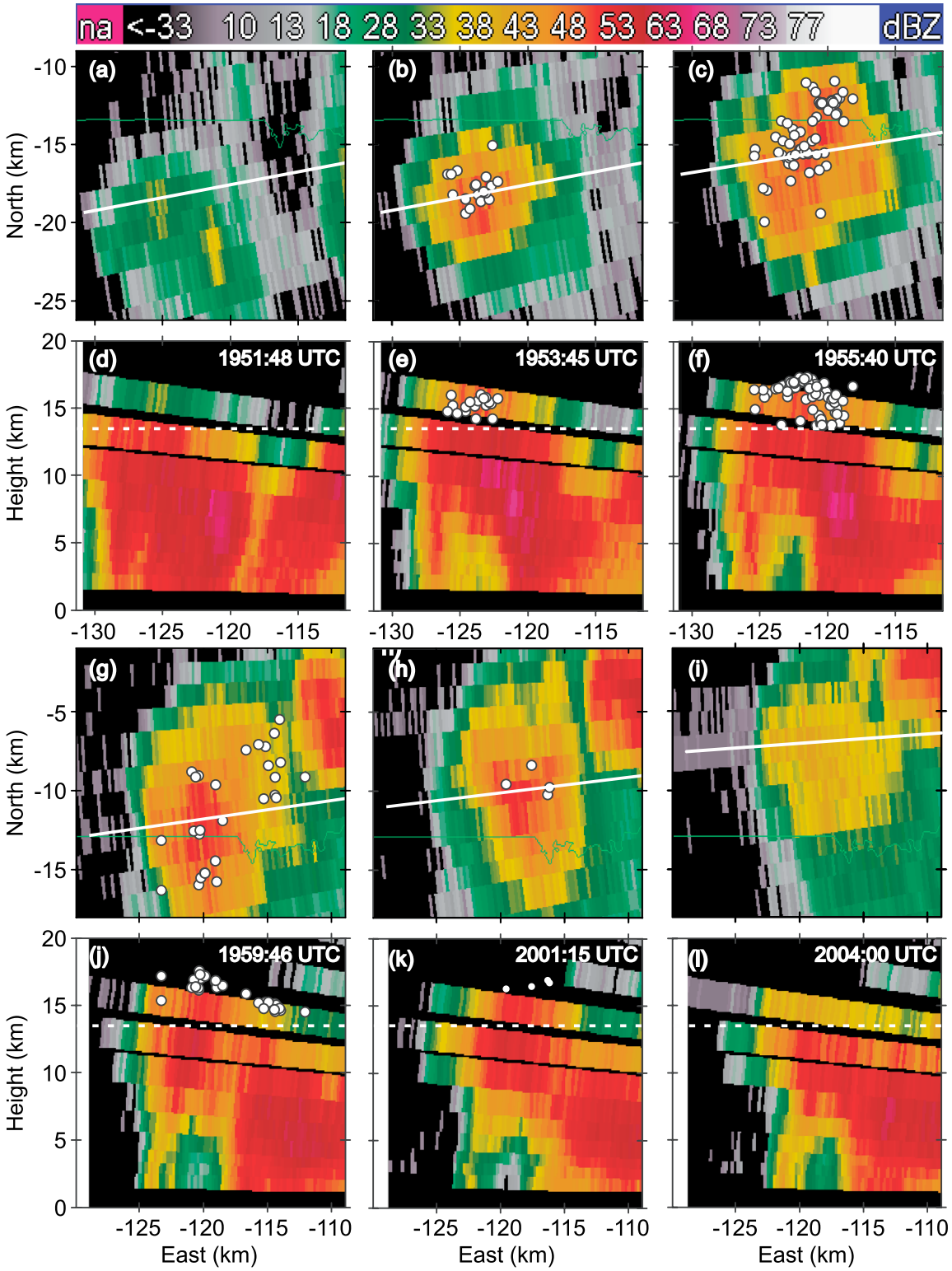

Figure 9. (a–l) Evolution of a VHF overshooting top signature relative to radar reflectivity structure from select volume scans of the NWRT PAR radar on 24 May 2011. Figures 9a–9c and 9g–9i show reflectivity from the 6.4° radar elevation angle, which is at an altitude of 14, 15, and 16 km msl at the right edge, middle, and left edge of the image. VHF sources began occurring above the LNB in this updraft pulse approximately 1 min after the 1951:48 volume scan and ceased by the 2004:00 UTC volume scan. The white line on the plan projection indicates where the corresponding vertical cross section (Figures 9d–9f and 9j–9l) was taken. VHF source points are shown only for those that occurred above the level of neutral buoyancy (dashed line) within the 1 min period centered on the radar time. Storm motion was to the northeast. Horizontal distance is relative to the location of the NWRT PAR.

To quantify the relationship between the maximum height of VHF sources and of the echo top of various reflectivity values during the period of the VHF overshooting top signature, the 99.99th percentile was chosen because it depicts the upper height of VHF sources well, but is insensitive to the few erroneous heights that can be produced by VHF Lightning Mapping Arrays. Figure 10 shows a scatterplot of the maximum heights of various reflectivity levels versus the heights of the 99.99th percentile during the VHF overshooting top signature for the three supercell storms. Solid lines show the linear fit and its associated 95% confidence levels for each panel. The two storms that were not supercells were omitted from this analysis because of the small number of radar observations during the short duration of their overshooting top signatures.

The 0.86–0.87 correlation coefficient for 18 dB*Z* echo tops indicates a strong positive relationship with the 99.99th percentile. The correlation coefficient tends to decrease with increasing reflectivity, although it remains ≥0.69 even for 50 dB*Z* for these three supercell storms. However, the correlation with the 60 dB*Z* echo tops is poor in two of the cases, and in the third case, with a correlation coefficient of 0.73, the regression line becomes more vertical.

The position of the linear fit relative to the dashed line indicates whether the height of the 99.99th percentile tended to be above, below, or coincident with that of the echo top of a particular reflectivity. The height of the 99.99th percentile was closest to the height of the 30 dB*Z* echo top for the two May cases and was closest to the height of the 18 dB*Z* echo top for the June case. As the value of reflectivity increased, the height of echo top tended to decrease, as expected, and its relationship to the 99.99th percentile tended to have more scatter about the linear fit.

6.3. Evolution of Lightning Height Relative to Overshooting Tops From IR Satellite Data

Figure 11 shows how the timing of the VHF overshooting top signature compares with the timing of an overshooting top in IR satellite imagery in four of the five cases. (In the fifth case the period between satellite images was too long relative to the duration of the VHF signature for a reasonable comparison.) In all four cases, the onset of the VHF overshooting top signature preceded the onset in IR imagery, and in one of those cases, a multicell storm, IR imagery never had an overshooting top. The relative timing for detecting a decline of the overshooting top in satellite imagery was mixed. In one case, the decline was outside the period of our analysis because it followed the merger of two storms (24 May 2011, Case 1). In one supercell storm (23–24 May 2011, Case 2), the end of the overshooting top in IR imagery preceded the end of the VHF signature, in the other supercell storm (1 June 2009, Case 3), the IR imagery maintained an overshooting top longer, and in the multicell case (7–8 April 2007, Case 4), the IR brightness temperature was always greater than that of the LNB, so the overshooting top was never detected by satellite, although the brightness temperature decreased through much of the analyzed period. Note that the greater frequency and spatial resolution of IR images produced by GOES-R likely will improve IR detection of overshooting tops and so would be expected to reduce the periods in which overshooting tops are missed in IR imagery.

7. Discussion and Summary

7.1. Overshooting Tops and Lightning Flash Rates Depicted by VHF Lightning Mapping Systems

As noted in section 1, early VHF lightning mapping data showed that discharges can penetrate above the level of neutral buoyancy (LNB) [*Krehbiel et al*., 2000; *Ushio et al*., 2003; *MacGorman et al*., 2005]. Subsequent studies of a supercell storm [*MacGorman et al*., 2008; *Calhoun et al*., 2013] showed that the VHF sources above the LNB typically were within the overshooting top and formed a secondary maximum in the vertical distribution of sources. *Emersic et al*. [2011], in a study of a multicell hailstorm, and *Calhoun et al*. [2013], in the supercell study, reported that the character of discharges in the overshooting top was unusual in that the VHF sources occurred continually at relatively low rates, without discernable channel structure (i.e., the discharges probably had very small spatial extent), independent of flashes at lower altitudes. This character of the high-altitude discharges probably was a result of a combination of two effects: the well-established decrease in the electric field threshold for initiating discharges with increasing altitude [e.g., *MacGorman and Rust*, 1998] and the smaller spatial scales for charge regions expected in the overshooting top. It remains unclear whether these discharges are related to the small transient luminous events (termed gnomes and pixies) that were observed visually on the periphery of an overshooting top by *Lyons et al*. [2003].

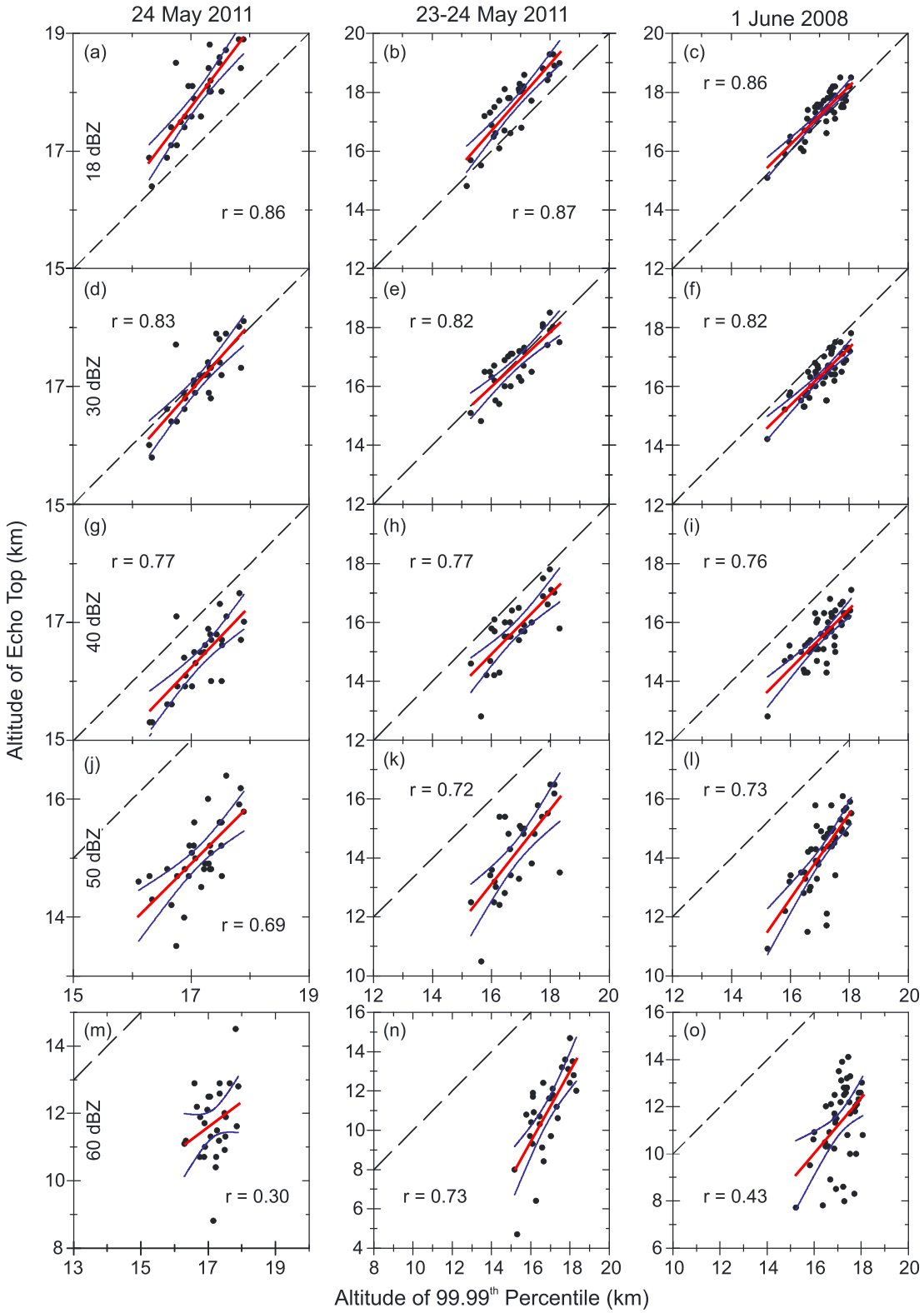

Figure 10. Correlation between the altitude of $LMA_{99.99}$ for VHF sources and the altitude of echo top for various radar reflectivity values in three supercell storms. The red line is the linear regression line for the points in each panel, and *r* is the correlation coefficient for that regression. Dark blue lines on either side of the regression line indicate the 95% confidence level. The dashed line is a reference line along which the altitude of echo top equals the altitude of $LMA_{99.99}$. The reflectivity value in the leftmost panel of each row applies to the echo top for all panels in the row. Note that the axis scales for the last two rows differ from those in the first three rows, and the scales change also from one storm to another.

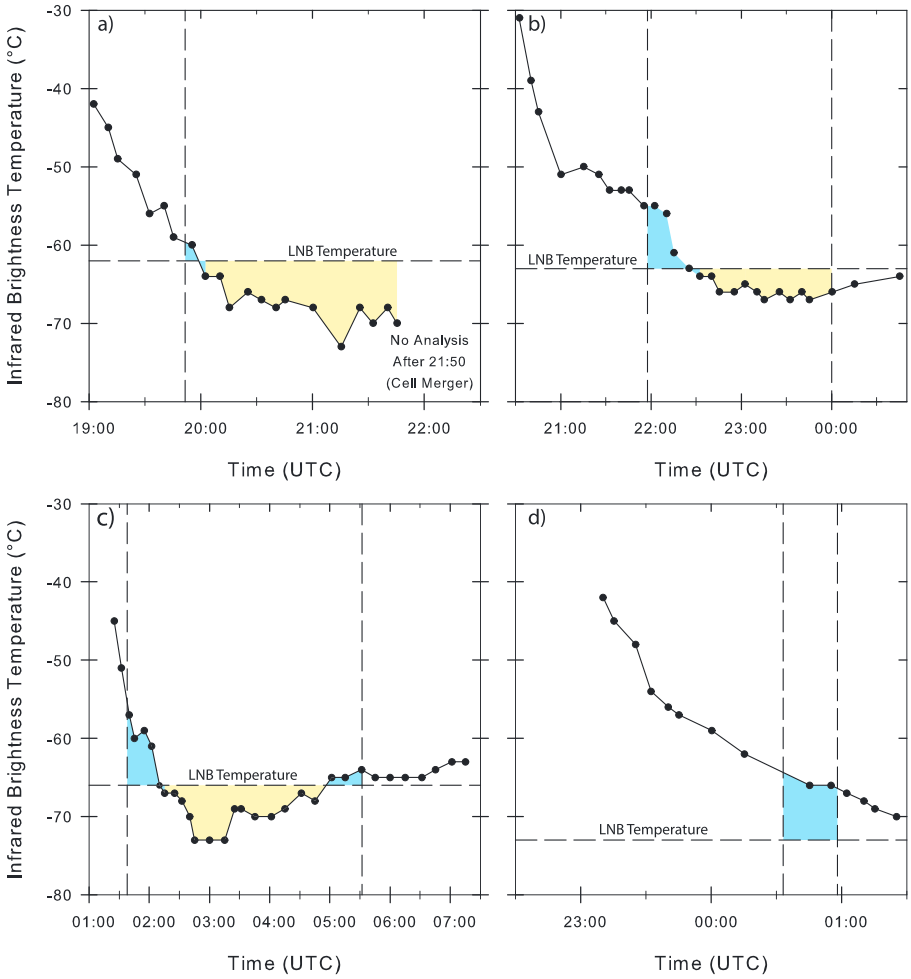

Figure 11. Satellite brightness temperature relative the equilibrium level (i.e., level of neutral buoyancy, horizontal dashed line labeled LNB) and the time of the overshooting top signature in VHF sources mapped by the OK-LMA (vertical dashed lines). (a) A tornadic supercell storm on 24 May 2011, (b) a nontornadic supercell storm on 23–24 May 2011, (c) a nontornadic supercell storm on 1 June 2009, and (d) a multicell storm on 7–8 April 2007.

In this study, we defined the VHF overshooting top signature as the period in which at least 4 VHF sources min^{-1} occurred in some 200 m layer above the LNB within a horizontal span comparable to the width of the overshooting top in reflectivity. Furthermore, we examined the evolution of VHF sources relative to the reflectivity structure and IR cloud tops of overshooting tops and relative to severe weather. To select cases for study, we reviewed data from the Oklahoma Lightning Mapping Array (OK-LMA) for tens of storms and found that, anytime VHF sources were consistently detected above the LNB for a few tens of minutes, the VHF sources above the LNB formed a secondary maximum in the vertical distribution of VHF sources and were clustered within a horizontal span of anywhere from a few kilometers up to roughly 10 km, often with a domed appearance, similar to the appearance of overshooting tops. The five cases analyzed in this study (one tornadic supercell storm, two nontornadic supercell storms, a strong multicell storm, and a large multicell storm that appeared to have weaker maximum updraft speeds) were chosen because they remained within coverage of the OK-LMA for most of their lifetime, were observed reasonably well by radar, and provided a spectrum of storm characteristics.

The behavior of lightning overall in these storms was similar to behavior documented previously in other storms. The durations of cycles in flash rates were similar to those for cycles in the altitude of echo top for moderate reflectivities, as would be expected from a common dependence on updraft cycles. A dependence on updraft cycles is further supported by the observation of sequential rising maxima of VHF source density in time-height plots during the early growth of the thunderstorms, similar to the

rising lightning bubbles observed by *Ushio et al*. [2003]. It also is supported by observational studies of lightning and kinematics in other storms [e.g., *MacGorman et al*., 1989; *Wiens et al*., 2005; *Calhoun et al*., 2013] and by storm simulations using numerical models explicitly incorporating electrification microphysics and lightning [e.g., *Mansell et al*., 2005, 2010; *Barthe and Pinty*, 2007; *Kuhlman et al*., 2006; *Calhoun et al*., 2014]. Thus, our conceptual model is of a rising parcel that contains the discharges emitting the VHF radiation, but the present study did not identify and track parcels in three dimensions to confirm this interpretation. Note that later increases in the altitude and density of VHF sources above the LNB in the present study sometimes did not appear to rise from lower levels, as they had done initially, but rather, simply appeared in the upper part of the overshooting top, although they could well still have been caused by updraft pulses.

Variations in the behavior of the "bubbles" likely are affected by variations in updrafts on two scales of time and space that can overlap: (1) the development of a relatively broad new updraft and (2) the faster variations of smaller regions of updraft maxima in the broader updraft. In some respects, this delineation is similar to the delineation of a spectrum of strong to weak evolution of updrafts noted by *Foote and Frank* [1983], who labeled the series of distinct updrafts in multicell storms strong evolution and the quasi-steady updrafts of supercell storms weak evolution. The evolution of maximum heights of VHF sources in the multicell storm on 7–8 September 2007 appears to have been dominated by strong evolution, with the altitude rising to a peak and falling in each of three cells peaking roughly 30 min apart.

The quasi-steady updrafts inferred from the VHF OT signatures of the supercell storms, however, were maintained for several hours and encompassed more rapid pulsing variations in the maximum height and in the elevated densities of VHF sources. Previous studies have shown that quasi-steady updrafts are maintained by a cycle in which the surface outflow from an existing updraft surges cyclonically around the updraft and creates an occlusion that blocks the inflow to its updraft and causes the formation of a new updraft, the complete cycle taking several tens of minutes [e.g., *Lemon and Doswell*, 1979]. However, *Foote and Frank* [1983] observed that a broad quasi-steady updraft contained smaller updraft variations, and *Doswell and Burgess* [1993] noted that supercell updrafts typically contain many smaller cellular updraft features, each lasting several minutes. Even relatively small cumulus clouds typically contain multiple updrafts overlapping in time as they grow [e.g., *Blyth et al*., 1988; *Blyth and Latham*, 1997]. Furthermore, in rapid-scan satellite imagery of cloud tops, *Mecikalski et al*. [2016] observed oscillations of cloud top temperature and height above the LNB lasting < 10 min; they also suggested that cases in which sequential oscillations of the cloud top rising above and falling below the height of glaciation over a period of a few minutes were caused by the rise and fall of successive turrets. The short pulsing variations we observed in the maximum height and in the upper density of VHF sources in the overshooting top are consistent with the oscillations in cloud top height observed by *Mecikalski et al*. [2016] and with the constantly evolving cellular structures comprising quasi-steady updrafts noted by *Doswell and Burgess* [1993].

Relatively little attention has been focused in the journal literature on these small, rapid updraft variations in studies of quasi-steady updrafts. However, some have suggested that regions of rapid variations in updraft speeds or regions of turbulence around the periphery of broad updrafts may be important to the microphysics of the storm [e.g., *Musil et al*., 1986]. Similarly, simulations of hydrometeor growth in cumulus clouds have found that observed characteristics were most consistent with results achieved by including the effects of multiple updrafts within the simulated cloud [e.g., *Blyth and Latham*, 1997]. Because most charge that produces discharges in the vicinity of updrafts is thought to have been produced by processes involved in precipitation growth, it may provide new information about updrafts and precipitation growth to attempt to identify rising parcels of greater VHF source density in overshooting tops and to trace them backward to their origin at lower altitudes relative to the microphysical structure inferred from polarimetric radar or from storm simulations.

7.2. VHF Overshooting Top Signature Relative to Overshooting Top From Radar and Satellite IR

The onset of the VHF signature typically occurred as 18 or 30 dB*Z* echo tops rose and were sustained above the LNB. Similarly, the end of the signature typically occurred near the time the 18 or 30 dB*Z* echo top fell below the LNB. The onset of the signature occurred before an overshooting top was apparent in satellite IR imagery, if it ever was apparent, but this difference may be lessened by the improved spatial and temporal resolution of IR imagery in the next generation of GOES satellites.

During the period in which the VHF signature was maintained, the timing of variations in the height of the 99.99th percentile of VHF sources ($LMA_{99.99}$) appeared similar to those of the echo tops of 18–40 dB*Z* reflectivities. A correlation analysis of the three supercell storms during the period of the VHF signature showed that the altitude of $LMA_{99.99}$ was well correlated with the altitude of 18–30 dB*Z* echo tops and was most similar to the altitude of 18 dB*Z* echo tops in one storm and to the altitude of 30 dB*Z* echo tops in the other two storms. (Data from the two multicell storms were insufficient during the VHF signature for a correlation analysis.)

7.3. Overshooting Top Signature Relative to Severe Weather

The initial occurrence of the VHF OT signature preceded an increase in the severity of either radar-inferred or actual storm hazards in each of the examined cases. While some marginally severe hail reports occurred before the onset of the signature in some cases, the majority of the severe events and the most violent events (e.g., largest hail and tornadoes) occurred while the signature was present. Furthermore, MESH, a radar-derived estimate of hail size independent of reports, was greatest during the VHF overshooting top signatures in each case. A pattern of $LMA_{99.99}$ collapse and subsequent relative minimum occurring just before tornadogenesis was shown for each of the tornadoes in Case 1. Although these observations are consistent with other studies that have documented the collapse of overshooting tops before tornado formation [e.g., *Lemon et al*., 1978; *Adler and Fenn*, 1981; *Steiger et al*., 2007; *Bedka et al*., 2010], the present $LMA_{99.99}$ sample size is too small for the VHF overshooting top relationship to be considered conclusive. Furthermore, while the onset of the VHF overshooting top signature was reasonably well timed with an increase in the severity of weather, no discernible patterns emerged between the subsequent fluctuations in either source densities or $LMA_{99.99}$ and variations in the intensity of the severe weather parameters. Nevertheless, the presence of a VHF overshooting top signature generally implied that severe weather was either imminent or occurring, especially when the signature extended well above the LNB.

It has been well documented that sudden increases in total lightning flash rates often occur prior to the onset of severe weather [e.g., *Goodman et al*., 1988; *MacGorman et al*., 1989; *Williams et al*., 1989, 1999; *Buechler et al*., 2000; *Lang et al*., 2000; *Goodman et al*., 2005; *Wiens et al*., 2005; *Tessendorf et al*., 2007; *Gatlin and Goodman*, 2010; *Darden et al*., 2010]. From an extensive evaluation of several criteria for an increase in the running average of flash rates by some multiple of the standard deviation, *Schultz et al*. [2011] suggested that using rapid increases in lightning flash rates (termed "lightning jumps") could improve lead times for severe weather warnings and reduce false alarms. The extent to which automated algorithms for detecting lightning jumps can aid severe storm warnings continues to be evaluated.

Note that when interpreting lightning jumps in large multicell storms, changes in the size and configuration of the storm system should be factored into the interpretation, as noted by *Schultz et al*. [2015]. Case 5 was the largest storm system but appeared to have weaker convective cells than the other cases had. Yet its larger total flash rates were comparable to those of the supercell storms, and some of its largest increases in flash rates occurred toward the end of the VHF overshooting top signature, when the storm system was weakening. As done in various quasi-operational evaluations of lightning jumps, it would have been necessary to consider lightning jumps only for the individual convective elements when considering their relationship to severe weather in Case 5.

Note also that unlike lightning jumps, increases in VHF source rates are often not related to increasing potential for severe weather, because source rates depend on the size of storms and on the average size of flashes, as well as on the characteristics of updrafts and precipitation growth. Furthermore, the fraction of VHF sources that are detected decreases rapidly with range [*Boccippio et al*., 2001], and our unpublished data indicate the VHF source rates are more strongly influenced by range than are flash rates. In the storms analyzed here, VHF source rates tended to increase with time as the storm became larger, and the largest VHF source rates occurred during the beginning of the storm's dissipation in three of the four storms whose dissipation stage was observed.

Each of the storms analyzed by this study had at least one increase in flash rates satisfying criteria for a lightning jump at some point during their lifetime. In the supercell storms (i.e., Cases 1–3) and in one of the multicell storms (i.e., Case 5), the lightning jumps (as well as the onset of the LMA overshooting top signature) were reasonably well timed with an increase in the severity of weather hazards and in radar-inferred estimates of

maximum hail size (no severe hail, i.e., > 2.5 cm in diameter, was reported in either multicell storm). However, the lightning jump lagged the onset of the VHF OT signature by 3 to almost 30 min for these four cases. In the other multicell storm (i.e., Case 4), the lightning jump lagged by 1 min the onset of severe hail potential indicated by MESH, while the VHF OT signature lagged it by 7 min. These results illustrate the potential utility of both VHF overshooting top signatures and lightning jumps to provide more confident warnings of severe weather hazards.

Nevertheless, at present, VHF OT signatures can be detected only by LMAs, which cover an extremely small fraction of the continental United States (CONUS). On the other hand, the GOES-R and GOES-S satellites will include Geostationary Lightning Mappers (GLMs) that will be able to detect lightning jumps over all of the contiguous United States and over much of the American hemisphere, including adjoining oceans. Thus, while VHF OT signatures might often detect the onset of severe weather in a storm earlier than lightning jumps do, the inability to observe them over large areas limits their effectiveness in the warning decision process.

7.4. Hypotheses Concerning Charge Regions Producing Overshooting Top Discharges

Observational studies have demonstrated that flashes typically are initiated by electrical breakdown of air in a region of large electric field magnitude, typically between a positive charge region and a negative charge region, and tend to propagate bidirectionally into these two regions, although additional charge regions may become involved, consistent with electrostatics [*Jacobson and Krider*, 1976; *MacGorman et al*., 1981, 2001, 2015; *Mazur and Ruhnke*, 1993; *Shao and Krehbiel*, 1996; *Coleman et al*., 2003; *Rust et al*., 2005; *Wiens et al*., 2005; *Weiss et al*., 2008; *Pilkey et al*., 2014]. Furthermore, *Williams et al*. [1985] showed that sparks propagating through plastic blocks doped with charge in various configurations tend to propagate preferentially, and to branch more heavily, in regions having greater charge density, and they presented scaling arguments to suggest that this is true also of lightning. These behaviors were also seen in later numerical simulations by *Mansell et al*. [2002, 2005] using a dielectric breakdown model of sparks and lightning. Note, too, that the electric field magnitude required to initiate a discharge decreases rapidly with altitude [*MacGorman and Rust*, 1998], so less charge likely would be needed to initiate discharges in overshooting tops.

Although electrodynamic processes certainly are involved in the details of lightning initiation and development, electrostatic theory is sufficient to explain the observed locations of flash initiation and the basic structure of flashes, as argued by several investigators [e.g., *Kasemir*, 1960; *MacGorman et al*., 1981, 2001; *Mazur and Ruhnke*, 1993; *Williams et al*., 1985]. As electrification processes increase the amount of charge in each of two adjoining regions of opposite polarity, the largest electric field magnitudes, where flash initiation is most likely, tend to occur between them. A discharge then propagates bidirectionally outward toward each charge region into weaker field magnitudes. Subsequent propagation in each charge region is maintained by the potential difference between the extremes of flash structure and the surrounding charge region and tends to be bounded by the well of electric potential in that region [*MacGorman et al*., 1981, 2001; *Mazur and Ruhnke*, 1993; *Mansell et al*., 2002; *Coleman et al*., 2003]. Together, the above observations are consistent with the reason for the small size and continual occurrence of discharges in overshooting tops being that small distinct concentrations of charge of one polarity are continually brought near concentrations of charge of the opposite polarity throughout much of the overshooting top.

We offer two hypotheses for the continual production of the small charge regions. Both involve charge being organized by kinematic structures as discussed by *Bruning and MacGorman* [2013], who investigated flashes at lower altitudes near an updraft. The hypotheses are not necessarily mutually exclusive; both could occur.

The first hypothesis, suggested previously by *MacGorman et al*. [2008], *Emersic et al*. [2011], and *Calhoun et al*. [2013], is that the discharges occur between (1) the charge lofted into the overshooting top by the strong updraft and (2) the screening-layer charge that forms on the upper cloud boundary. The charge lofted by the updraft is produced by electrification processes lower in the storm. The screening-layer charge, produced by the discontinuity in electric conductivity at the cloud boundary [*Hoppel and Phillips*, 1971; *Brown et al*., 1971; *MacGorman and Rust*, 1998], reaches 60% of its equilibrium value quickly at cloud top after a change in the electric field inside the cloud boundary (within roughly 10 s at 15 km and 2 s at 20 km). These investigators suggested that the grape-cluster appearance of the overshooting top would organize the

screening-layer charge by quasi-periodically folding the charge inward, closer to the charge lofted by the updraft, a process similar to the motions of upper cloud boundaries observed by *Blyth et al*. [1988] and *Stith* [1992]. The distance scale at which the screening-layer charge is brought closer to the internal charge would be approximately the same as the distance between the lumps apparent in the cloud boundary, caused at least in part by interaction of the updraft with the horizontal winds at that level.

The second hypothesis involves the increasing hydrometeor number concentration caused by the decrease in updraft speeds with increasing height in the overshooting top. Investigators have previously noted that the decrease in updraft speeds with height leads to accumulations of graupel or snow, especially as the particles approach updraft speeds that have decreased to approximately the terminal fall speed of the particle [*Lhermitte and Williams*, 1985; *Ziegler et al*., 1991; *Randell et al*., 1994]. Values of radar reflectivity of 30 dB*Z* or more, sometimes much more, extended into the overshooting top in all cases we observed, and the maximum height of VHF sources correlated well with the maximum height of 30 dB*Z* within overshooting tops. Values of reflectivity $\geq$30 dB*Z* typically indicate the presence of graupel-sized particles, which would be expected to carry charge opposite in polarity to the charge produced previously by the noninductive graupel-ice mechanism on smaller, higher ice particles, if they gained the charge in the mixed-phase region. The vertical gradient in reflectivity is large in the overshooting top, so the charge on graupel-sized particles is brought relatively close to the charge on smaller ice particles. In this scenario, the relatively small size of the charge regions involved in the discharges could be due to variations in updraft speeds over horizontal distances of roughly1–2 km or less or could be due to large gradients in particle number density. Recent balloon-borne soundings of hydrometeor size and number in two storms found number densities of small ice particles varying by 1–2 orders of magnitude from one 50 m interval of height to the next and large variations occurred also over larger intervals of height [*Waugh*, 2016].

One might expect that the polarity of charge carried by the small ice particles lofted into the overshooting top would be the same as the polarity of charge carried by small particles in the upper part of most of the rest of the storm: positive in typical storms [see *MacGorman and Rust*, 1998, discussion, pp. 49–53] and negative in storms dominated by an anomalous vertical charge distribution, such as storms studied, for example, by *Rust et al*. [2005], *MacGorman et al*. [2005], *Wiens et al*. [2005], *Tessendorf et al*. [2007], and *Weiss et al*. [2008]. While this may be true of all or most anomalous storms, it may not be true of many of the strong storms dominated by more typical charge distributions. Most hypotheses for producing storms with anomalous charge distributions [e.g., *Williams et al*., 2005; *MacGorman et al*., 2011] have involved unusually large liquid water contents in the mixed-phase region of the updraft, because laboratory experiments have found that graupel gains positive charge, instead of the usual negative charge, when riming graupel collides with and rebounds from small ice particles in the presence of large liquid water contents [e.g., *Takahashi and Miyawaki*, 2002; *Emersic and Saunders*, 2010].

However, several studies have suggested that the polarity of charge gained by graupel may vary across the updraft, because of variations in updraft properties affecting the polarity [*MacGorman et al*., 2005, 2011; *Kuhlman et al*., 2006; *Emersic et al*., 2011; *Bruning et al*., 2014]. The air in overshooting tops is air that has attained a storm's greatest updraft velocities; it tends to be air in the updraft core, which has less entrainment and mixing with drier or cooler air [e.g., *Musil et al*., 1986, 1991] and might be expected to have had less precipitation growth at altitudes below the mixed-phase region than air on the periphery of the updraft. Thus, it would also realize the largest fraction of the storm's adiabatic potential for liquid water [e.g., *Musil et al*., 1986, 1991] and could have enough liquid water content for positive charging of graupel, resulting in a core having an anomalous vertical distribution of charge (i.e., the upper main charge is negative), even if the rest of the updraft does not. This provides an alternative explanation for the uppermost negative charge in the conceptual model for strong updrafts by *Stolzenburg et al*. [1998], which was attributed to a screening layer. Instead, diverging flow from closer to the updraft core in the upper part of a strong storm could often carry negative charge horizontally from the region of the updraft core.

It seems reasonable to us, then, that the interior charge in the weaker reflectivities ($<$30 dB*Z*) of the overshooting top of many strong storms may be negative, even if most of the upper part of the storm has the more typical positive particle charge. If so, then the spectrum of speeds and widths and of other characteristics affecting liquid water content that are possible in storm updrafts would lead to a corresponding spectrum in the fraction of a storm updraft having anomalous charging of graupel, ranging from none of the

updraft, to updrafts with only small anomalous regions, to the storms dominated by anomalous regions that have been the object of most studies of so-called inverted-polarity storms. Note that having opposite polarities of particle charging across a relatively short horizontal span of strong gradients in the updraft may also contribute to the very large rate of small flashes typically observed around the updraft of supercell storms.

The limitations of available observing systems make it very difficult to obtain observations establishing what actually occurs in overshooting tops. The altitude of most overshooting tops is higher than the operating ceiling of all currently available storm-penetrating aircraft, and the overshooting top is, at best, an extremely difficult target to hit with a balloon launched from the ground. The best chance to make in situ measurements of the overshooting top may be to launch an extensive array of many small, cheap balloon-borne electric field sensors, a strategy that may become possible with technologies now being developed. If an aircraft with a sufficiently high ceiling for overflights were able to release dropsondes, then having suitable dropsonde instruments for measuring storm electric fields would provide another option.

It may also be possible now to obtain indirect support remotely from existing VHF time-of-arrival and interferometer mapping systems [e.g., *Rison et al*., 1999; *Rhodes et al*., 1994; *Shao et al*., 1996; *Stock et al*., 2014]. *Rison et al*. [2016] showed that the process initiating many, and perhaps all, flashes was a system of faint positive streamers developing toward negative charge, followed by self-propagating negative leaders that formed near the origin of the streamers and propagated toward and into positive charge and additional positive leaders that propagated toward and into negative charge. Paul Krehbiel (New Mexico Tech, private communication, 2016) has suggested that the VHF sources from discharges in the overshooting top are consistent with the system of positive streamers that *Rison et al*. [2016] found had initiated many flashes. Based on *Rison et al*.'s [2016] observations of the positive streamers, he noted that like the overshooting top discharges, the positive streamers have small spatial extent (roughly 500 m), and the VHF sources have a wide range of radiated power, comparable to that from the subsequent stages of flashes.

The 1 μs time resolution of the interferometer data is sufficient to determine the direction of development of the system of positive streamers, but the present interferometer has a limited useful horizontal range (roughly $<$20–40 km, depending on its baseline length). If the updraft of a supercell storm occurs within range of the system and also within range of dual-Doppler radars capable of providing updraft velocities, it should be possible to determine the propagation direction of the small flashes and their location relative to the updraft. If the small frequent flashes around middle levels of the updraft discharge positive charge in the updraft core, as hypothesized above, this would also imply that the uppermost charge rising in the updraft core into the overshooting top is negative. Similarly, if an overshooting top occurs within range of the VHF interferometer, within the range for three-dimensional coverage of the OK-LMA, and within range of a radar scanning that high, it should be possible to determine the direction, from positive toward negative charge, of discharges in the overshooting top and to infer whether they discharge only internal charges across the interface between moderate and low reflectivity values, discharge between screening-layer charge and an internal charge, or do both.

Acknowledgments

Oklahoma Lightning Mapping Array data are available from don.macgorman@noaa.gov or from kristin.kuhlman@noaa.gov. Funding for this research was provided by National Science Foundation grants AGS-0924621 and AGS-1063945, by NOAA/NESDIS grant L2NSR20PCF, and by NOAA/Office of Oceanic and Atmospheric Research under NOAA-University of Oklahoma Cooperative Agreement NA11OAR4320072, U.S. Department of Commerce. Many provided technical support or shared their considerable radar or lightning expertise with us for this study, and we thank them: Paul Krehbiel, Eric Bruning, and Kristin Calhoun provided helpful discussions and insights concerning lightning data. Conrad Ziegler shared insights concerning updraft kinematics. Terry Schuur, Matt Kumjian, and Pam Heinselman shared their radar expertise. Valliappa Lakshmanan, Kevin Manross, Kevin Haghi, Patrick Marsh, and Kristin Calhoun provided assistance with various analysis packages. Steve Fletcher and Will Agent kept workstations and software packages running, and Dennis Nealson and Doug Kennedy kept the Lightning Mapping Array operating. We also appreciate the helpful comments in a review of a preliminary manuscript by Ted Mansell and in reviews of the journal submission by John Pilkey and two anonymous reviewers.

References

Adler, R. F., and D. D. Fenn (1981), Satellite-observed cloud-top height changes in tornadic thunderstorms, *J. Appl. Meteorol.*, *20*, 1369–1375.

Barth, M. C., et al. (2015), Overview of the Deep Convective Clouds and Chemistry (DC3) field campaign, *Bull. Am. Meteorol. Soc.*, *96*, 1281–1309, doi:10.1175/BAMS-D-13-00290.1.

Barthe, C., and J.-P. Pinty (2007), Simulation of a supercellular storm using a three-dimensional mesoscale model with an explicit lightning flash scheme, *J. Geophys. Res.*, *112*, D06210, doi:10.1029/2006JD007484.

Bedka, K. M., W. F. Feltz, J. R. Mecikalksi, R. D. Sharman, A. Lenz, and J. Gerth (2010), Objective satellite-based detection of overshooting tops using infrared window channel brightness temperature gradients, *J. Appl. Meteorol. Climatol.*, *49*, 181–201, doi:10.1175/2009JAMC2286.1.

Benjamin, S. G., et al. (2004), An hourly assimilation-forecast cycle: The RUC, *Mon. Weather Rev.*, *132*, 495–518.

Blyth, A. M., and J. Latham (1997), A multi-thermal model of cumulus glaciation via the Hallett-Mossop process, *Q. J. R. Meteorol. Soc.*, *123*, 1185–1198.

Blyth, A. M., W. A. Cooper, and J. B. Jensen (1988), A study of the source of entrained air in Montana cumuli, *J. Atmos. Sci.*, *45*, 3944–3964.

Boccippio, D. J., S. Heckman, and S. J. Goodman (2001), A diagnostic analysis of the Kennedy Space Center LDAR network: 1. Data characteristics, *J. Geophys. Res.*, *106*, 4769–4786, doi:10.1029/2000JD900687.

Brock, F. V., K. C. Crawford, R. L. Elliott, G. W. Cuperus, S. J. Stadler, H. L. Johnson, and M. D. Eilts (1995), The Oklahoma Mesonet: A technical overview, *J. Atmos. Oceanic Technol.*, *12*, 5–19.

Brown, K. A., P. R. Krehbiel, C. B. Moore, and G. N. Sargent (1971), Electrical screening layers around charged clouds, *J. Geophys. Res.*, *76*, 2825–2835, doi:10.1029/JC076i012p02825.

Brown, R. A., V. T. Wood, and D. Sirmans (2002), Improved tornado detection using simulated and actual WSR-88D data with enhanced resolution, *J. Atmos. Oceanic Technol.*, *19*, 1759–1771.

Brown, R. A., B. A. Flickinger, E. Forren, D. M. Schultz, D. Sirmans, P. L. Spencer, V. T. Wood, and C. L. Ziegler (2005), Improved detection of severe storms using experimental fine-resolution WSR-88D measurements, *Weather Forecasting*, *20*, 3–14.

Bruning, E. C., and D. R. MacGorman (2013), Theory and observations of controls on lightning flash size spectra, *J. Atmos. Sci.*, *70*, 4012–4029, doi:10.1175/JAS-D-12-0289.1.

Bruning, E. C., W. D. Rust, D. R. MacGorman, M. I. Biggerstaff, and T. J. Schuur (2010), Formation of charge structures in a supercell, *Mon. Weather Rev.*, *138*, 3740–3761, doi:10.1175/2010MWR3160.1.

Bruning, E. C., S. A. Weiss, and K. M. Calhoun (2014), Continuous variability in thunderstorm primary electrification and an evaluation of inverted-polarity terminology, *Atmos. Res.*, *135–136*, 274–284, doi:10.1016/j.atmosres.2012.10.009.

Buechler, D. E., K. T. Driscoll, S. J. Goodman, and H. J. Christian (2000), Lightning activity within a tornadic thunderstorm observed by the Optical Transient Detector (OTD), *Geophys. Res. Lett.*, *27*, 2253–2256, doi:10.1029/2000GL011579.

Calhoun, K. M., D. R. MacGorman, C. L. Ziegler, and M. I. Biggerstaff (2013), Evolution of lightning activity and storm charge relative to dual-Doppler analysis of a high-precipitation supercell storm, *Mon. Weather Rev.*, *141*, 2199–2223, doi:10.1175/MWR-D-12-00258.1.

Calhoun, K. M., E. R. Mansell, D. R. MacGorman, and D. C. Dowell (2014), Numerical simulations of lightning and storm charge of the 29–30 May 2004 Geary, Oklahoma supercell thunderstorm using EnKF mobile radar data assimilation, *Mon. Weather Rev.*, *142*, 3977–3997, doi:10.1175/MWR-D-13-00403.1.

Chmielewski, V. C., and E. C. Bruning (2016), Lightning Mapping Array flash detection performance with variable receiver thresholds, *J. Geophys. Res. Atmos.*, *121*, 8600–8614, doi:10.1002/2016JD025159.

Chronis, T., L. D. Carey, C. J. Schultz, E. V. Schultz, K. M. Calhoun, and S. J. Goodman (2015), Exploring lightning jump characteristics, *Weather Forecasting*, *30*, 23–37, doi:10.1175/WAF-D-14-00064.1.

Coleman, L. M., T. C. Marshall, M. Stolzenburg, T. Hamlin, P. R. Krehbiel, W. Rison, and R. J. Thomas (2003), Effects of charge and electrostatic potential on lightning propagation, *J. Geophys. Res.*, *108*(D9), 4298, doi:10.1029/2002JD002718.

Crum, T. D., and R. L. Alberty (1993), The WSR-88D and the WSR-88D operation support facility, *Bull. Am. Meteorol. Soc.*, *74*, 1669–1687.

Darden, C. B., D. J. Nadler, B. C. Carcione, R. J. Blakeslee, G. T. Stano, and D. E. Buechler (2010), Utilizing total lightning information to diagnose convective trends, *Bull. Am. Meteorol. Soc.*, *91*, 167–175, doi:10.1175/2009BAMS2808.1.

Doswell, C. A., III, and D. W. Burgess (1993), Tornadoes and tornadic storms: A review of conceptual models, in *The Tornado: Its Structure, Dynamics, Prediction, and Hazards*, edited by C. Church et al., pp. 161–172, AGU, Washington, D. C.

Doviak, R. J., V. Bringi, A. Ryzhkov, A. Zahrai, and D. Zrnić (2000), Considerations for polarimetric upgrades to operational WSR-88D radars, *J. Atmos. Oceanic Technol.*, *17*, 257–278.

Dworak, R., K. Bedka, J. Brunner, and W. Feltz (2012), Comparison between GOES-12 overshooting top detections, WSR-88D radar reflectivity, and severe storm reports, *Weather Forecasting*, *27*, 684–699, doi:10.1175/WAF-D-11-00070.1.

Emersic, C., and C. P. R. Saunders (2010), Further laboratory investigations into the Relative Diffusional Growth Rate theory of thunderstorm electrification, *Atmos. Res.*, *98*, 327–340, doi:10.1016/j.atmosres.2010.07.011.

Emersic, C., P. L. Heinselman, D. R. MacGorman, and E. C. Bruning (2011), Lightning activity in a hail-producing storm observed with phased-array radar, *Mon. Weather Rev.*, *139*, 1809–1825, doi:10.1175/2010MWR3574.1.

Foote, G. B., and H. W. Frank (1983), Case study of a hailstorm in Colorado. Part III: Airflow from triple-Doppler measurements, *J. Atmos. Sci.*, *40*, 686–707.

Gatlin, P. N., and S. J. Goodman (2010), A total lightning trending algorithm to identify severe thunderstorms, *J. Atmos. Oceanic Technol.*, *27*, 3–22, doi:10.1175/2009JTECHA1286.1.

Goodman, S. J., D. E. Buechler, P. D. Wright, and W. D. Rust (1988), Lightning and precipitation history of a microburst-producing storm, *Geophys. Res. Lett.*, *15*, 1185–1188, doi:10.1029/GL015i011p01185.

Goodman, S. J., et al. (2005), The North Alabama Lightning Mapping Array: Recent severe storm observations and future prospects, *Atmos. Res.*, *76*, 423–437.

Hart, J. A., and W. Korotky (1991), The SHARP workstation vl.50 user's guide. NOAA/National Weather Service. 30 pp., NWS Eastern Region Headquarters, Bohemia, New York.

Heinselman, P. L., and S. M. Torres (2011), High-temporal-resolution capabilities of the national weather radar testbed phased-array radar, *J. Appl. Meteorol. Climatol.*, *50*, 579–593, doi:10.1175/2010JAMC2588.1.

Hoppel, W. A., and B. B. Phillips (1971), The electrical shielding layer around charged clouds and its role in thunderstorm electricity, *J. Atmos. Sci.*, *28*, 1258–1271.

Jacobson, E. A., and E. P. Krider (1976), Electrostatic field changes produced by Florida lightning, *J. Atmos. Sci.*, *33*, 103–117.

Kasemir, H. W. (1960), A contribution to the electrostatic theory of a lightning discharge, *J. Geophys. Res.*, *65*, 1873–78, doi:10.1029/JZ065i007p01873.

Krehbiel, P. R., R. J. Thomas, W. Rison, T. Hamlin, J. Harlin, and M. Davis (2000), GPS-based mapping system reveals lightning inside storms, *Eos, Trans. AGU*, *81*, 21–25.

Kuhlman, K. M., C. L. Ziegler, E. R. Mansell, D. R. MacGorman, and J. M. Straka (2006), Numerically simulated electrification and lightning of the 29 June 2000 STEPS supercell storm, *Mon. Weather Rev.*, *134*, 2734–2757.

Kumjian, M. R., A. V. Ryzhiov, V. M. Melnikov, and T. J. Schuur (2010), Rapid-scan super-resolution observations of a cyclic supercell with a dual-polarization WSR-88D, *Mon. Weather Rev.*, *138*, 3762–3786, doi:10.1175/2010MWR3322.1.

Lakshmanan, V., T. Smith, K. Hondl, G. J. Stumpf, and A. Witt (2006), A real-time, three-dimensional, rapidly updating, heterogeneous radar merger technique for reflectivity, velocity, and derived products, *Weather Forecasting*, *21*, 802–823.

Lakshmanan, V., T. Smith, G. J. Stumpf, and K. Hondl (2007), The warning decision support system-integrated information, *Weather Forecasting*, *22*, 596–612, doi:10.1175/WAF1009.1.

Lakshmanan, V., K. Hondl, C. K. Potvin, and D. Preignitz (2013), An improved method for estimating radar echo-top height, *Weather Forecasting*, *28*, 481–488, doi:10.1175/WAF-D-12-00084.1.

Lang, T. J., S. A. Rutledge, J. E. Dye, M. Venticinque, P. Laroche, and E. Defer (2000), Anomalously low negative cloud-to-ground lightning flash rates in intense convective storms observed during STERAO-A, *Mon. Weather Rev.*, *128*, 160–173.

Lang, T. J., et al. (2017), WMO world record lightning extremes: Longest detected flash distance and longest detected flash duration. *Bull. Am. Meteorol. Soc.*, doi:10.1175/BAMS-D-16-0061.1, in press.

Lemon, L. R., and C. A. Doswell III (1979), Severe thunderstorm evolution and mesocyclone structure as related to tonadogenesis, *Mon. Weather Rev.*, *107*, 1184–1197.

Lemon, L. R., D. W. Burgess, and R. A. Brown (1978), Tornadic storm airflow and morphology derived from single-Doppler radar measurements, *Mon. Weather Rev.*, *106*, 48–61.

Lhermitte, R., and E. Williams (1985), Thunderstorm electrification: A case study, *J. Geophys. Res.*, *90*, 6071–6078, doi:10.1029/JD090iD04p06071.

Lhermitte, R., and P. R. Krehbiel (1979), Doppler radar and radio observations of thunderstorms, *IEEE Trans. Geosci. Electron.*, *GE-17*, 162–171.
Lyons, W. A., T. E. Nelson, R. A. Armstrong, V. P. Pasko, and M. A. Stanley (2003), Upward electrical discharges from thunderstorm tops, *Bull. Am. Meteorol. Soc.*, *84*, 445–454.
MacGorman, D. R., and W. D. Rust (1998), *The Electrical Nature of Storms*, pp. 422, Oxford Univ. Press, New York.
MacGorman, D. R., A. A. Few, and T. L. Teer (1981), Layered lightning activity, *J. Geophys. Res.*, *86*, 9900–9910, doi:10.1029/JC086iC10p09900.
MacGorman, D. R., D. W. Burgess, V. Mazur, W. D. Rust, W. L. Taylor, and B. C. Johnson (1989), Lightning rates relative to tornadic storm evolution on 22 May 1981, *J. Atmos. Sci.*, *46*, 221–250.
MacGorman, D. R., J. M. Straka, and C. L. Ziegler (2001), A lightning parameterization for numerical cloud models, *J. Appl. Meteorol.*, *40*, 459–478.
MacGorman, D. R., W. D. Rust, P. Krehbiel, W. Rison, E. Bruning, and K. Wiens (2005), The electrical structure of two supercell storms during STEPS, *Mon. Weather Rev.*, *133*, 2583–2607.
MacGorman, D. R., et al. (2008), TELEX: The thunderstorm electrification and lightning experiment, *Bull. Am. Meteorol. Soc.*, *89*, 997–1013, doi:10.1175/2007BAMS2352.1.
MacGorman, D. R., I. R. Apostolakopoulos, N. R. Lund, N. W. S. Demetriades, M. J. Murphy, and P. R. Krehbiel (2011), The timing of cloud-to-ground lightning relative to total lightning activity, *Mon. Weather Rev.*, *139*, 3871–3886, doi:10.1175/MWR-D-11-00047.1.
MacGorman, D. R., M. I. Biggerstaff, S. Waugh, J. T. Pilkey, M. A. Uman, D. M. Jordan, T. Ngin, W. R. Gamerota, G. Carrie, and P. Hyland (2015), Coordinated lightning, balloon-borne electric field, and radar observations of a triggered lightning flash in North Florida, *Geophys. Res. Lett.*, *42*, 5635–5643, doi:10.1002/2015GL064203.
Mansell, E. R., D. R. MacGorman, C. L. Ziegler, and J. M. Straka (2002), Simulated three-dimensional branched lightning in a numerical thunderstorm model, *J. Geophys. Res.*, *107*(D9), 4075, doi:10.1029/2000JD000244.
Mansell, E. R., D. R. MacGorman, C. L. Ziegler, and J. M. Straka (2005), Charge structure in a simulated multicell thunderstorm, *J. Geophys. Res.*, *110*, D12101, doi:10.1029/2004JD005287.
Mansell, E. R., C. L. Ziegler, and E. C. Bruning (2010), Simulated electrification of a small thunderstorm with two-moment bulk microphysics, *J. Atmos. Sci.*, *67*, 171–194, doi:10.1175/2009JAS2965.1.
Mazur, V., and L. Ruhnke (1993), Common physical processes in natural and artificially triggered lightning, *J. Geophys. Res.*, *98*, 12,913–12,930, doi:10.1029/93JD00626.
Mecikalski, J. R., C. P. Jewett, J. M. Apke, and L. D. Carey (2016), Analysis of cumulus cloud updrafts as observed with 1-min resolution super rapid scan GOES imagery, *Mon. Weather Rev.*, *144*, 811–830, doi:10.1175/MWR-D-14-00399.1.
Musil, D. J., A. J. Heymsfield, and P. L. Smith (1986), Microphysical characteristics of a well-developed weak echo region in a High Plains supercell thunderstorm, *J. Climate Appl. Meteorol.*, *25*, 1037–1051.
Musil, D. J., S. A. Christopher, R. A. Deola, and P. L. Smith (1991), Some interior observations of southeastern Montana hailstorms, *J. Appl. Meteorol.*, *30*, 1596–1612.
Ortega, K. L., T. M. Smith, K. L. Manross, K. A. Scharfenberg, A. Witt, A. G. Kolodziej, and J. J. Gourley (2009), The severe hazards analysis and verification experiment, *Bull. Am. Meteorol. Soc.*, *90*, 1519–1530, doi:10.1175/2009BAMS2815.1.
Pilkey, J. T., M. A. Uman, J. D. Hill, T. Ngin, W. R. Gamerota, D. M. Jordan, J. Caicedo, and B. Hare (2014), Rocket-triggered lightning propagation paths relative to preceding natural lightning activity and inferred cloud charge, *J. Geophys. Res. Atmos.*, *119*, 13,427–13,456, doi:10.1002/2014JD022139.
Randell, S. C., S. A. Rutledge, R. D. Farley, and J. H. Helsdon Jr. (1994), A modeling study on the early electrical development of tropical convection: Continental and oceanic (monsoon) storms, *Mon. Weather Rev.*, *122*, 1852–1877.
Rhodes, C. T., X. M. Shao, P. R. Krehbiel, R. J. Thomas, and C. O. Hayenga (1994), Observations of lightning phenomena using radio interferometry, *J. Geophys. Res.*, *99*, 13,059–13,082, doi:10.1029/94JD00318.
Rison, W., R. J. Thomas, P. R. Krehbiel, T. Hamlin, and J. Harlin (1999), A GPS-based three-dimensional lightning mapping system: Initial observations in central New Mexico, *Geophys. Res. Lett.*, *26*, 3573–3576, doi:10.1029/1999GL010856.
Rison, W., P. R. Krehbiel, M. G. Stock, H. E. Edens, X.-M. Shao, R. J. Thomas, M. A. Stanley, and Y. Zhang (2016), Observations of narrow bipolar events reveal how lightning is initiated in thunderstorms, *Nat. Commun.*, *7*, 10721, doi:10.1038/ncomms10721.|.
Rust, W. D., D. R. MacGorman, E. C. Bruning, S. A. Weiss, P. R. Krehbiel, R. J. Thomas, W. Rison, T. Hamlin, and J. Harlin (2005), Inverted-polarity electrical structures in thunderstorms in the Severe Thunderstorm Electrification and Precipitation Study (STEPS), *Atmos. Res.*, *76*, 247–271, doi:10.1016/j.atmosres.2004.11.029.
Ryzhkov, A. V., T. J. Schuur, D. W. Burgess, P. L. Heinselman, S. E. Giangrade, and D. S. Zrnić (2005), The joint polarization experiment: Polarimetric rainfall measurements and hydrometeor classification, *Bull. Am. Meteorol. Soc.*, *86*, 809–824.
Schultz, C. J., W. A. Petersen, and L. D. Carey (2011), Lightning and severe weather: A comparison between total and cloud-to-ground lightning trends, *Weather Forecasting*, *26*, 744–755, doi:10.1175/WAF-D-10-05026.1.
Schultz, C. J., L. D. Carey, E. V. Schultz, and R. J. Blakeslee (2015), Insight into the kinematic and microphysical processes that control lightning jumps, *Weather Forecasting*, *30*, 1591–1621, doi:10.1175/WAF-D-14-00147.1.
Shao, X. M., and P. R. Krehbiel (1996), The spatial and temporal development of intracloud lightning, *J. Geophys. Res.*, *101*, 641–668.
Shao, X. M., D. N. Holden, and C. T. Rhodes (1996), Broad band radio interferometry for lightning observations, *Geophys. Res. Lett.*, *23*, 1917–1929, doi:10.1029/96GL00474.
Steiger, S. M., R. E. Orville, and L. D. Carey (2007), Total lightning signatures of thunderstorm intensity over North Texas. Part I: Supercells, *Mon. Weather Rev.*, *135*, 3281–3302, doi:10.1175/MWR3472.1.
Stith, J. L. (1992), Observations of cloud-top entrainment in cumuli, *J. Atmos. Sci.*, *49*, 1334–1347.
Stock, M. G., M. Akita, P. R. Krehbiel, W. Rison, H. E. Edens, Z. Kawasaki, and M. A. Stanley (2014), Continuous broadband digital interferometry of lightning using a generalized cross-correlation algorithm, *J. Geophys. Res. Atmos.*, *119*, 3134–3165, doi:10.1002/2013JD020217.
Stolzenburg, M., W. D. Rust, and T. C. Marshall (1998), Electrical structure in thunderstorm convective regions. 3. Synthesis, *J. Geophys. Res.*, *103*, 14,097–14,108, doi:10.1029/97JD03545.
Takahashi, T., and K. Miyawaki (2002), Reexamination of riming electrification in a wind tunnel, *J. Atmos. Sci.*, *59*, 1018–1025, doi:10.1175/1520-0469.
Tessendorf, S. A., K. C. Wiens, and S. A. Rutledge (2007), Radar and lightning observations of the 3 June 2000 electrically inverted storm from STEPS, *Mon. Weather Rev.*, *135*, 3665–3681, doi:10.1175/2007MWR1954.1.
Thomas, R., P. Krehbiel, W. Rison, S. Hunyady, W. Winn, T. Hamlin, and J. Harlin (2004), Accuracy of the lightning mapping array, *J. Geophys. Res.*, *109*, D14207, doi:10.1029/2004JD004549.
Ushio, T., S. J. Heckman, H. J. Christian, and Z. I. Kawasaki (2003), Vertical development of lightning activity observed by the LDAR system: Lightning bubbles, *J. Appl. Meteorol.*, *42*, 165–174.

Waugh, S. M. (2016), A balloon-borne particle size, imaging, and velocity probe for in situ microphysical measurements, PhD dissertation, 187 pp., Univ. of Oklahoma, Norman.

Weiss, S., W. D. Rust, D. R. MacGorman, E. Bruning, and P. Krehbiel (2008), Evolving complex electrical structure of the STEPS 25 June 2000 multicell storm, *Mon. Weather Rev.*, *136*, 741–756, doi:10.1175/2007MWR2023.1.

Wiens, K. C., S. A. Rutledge, and S. A. Tessendorf (2005), The 29 June 2000 supercell observed during STEPS. Part II: Lightning and charge structure, *J. Atmos. Sci.*, *62*, 4151–4177.

Williams, E. R., C. M. Cooke, and K. A. Wright (1985), Electrical discharge propagation in and around space charge clouds, *J. Geophys. Res.*, *90*, 6059–6070, doi:10.1029/JD090iD04p06059.

Williams, E. R., M. E. Weber, and R. E. Orville (1989), The relationship between lightning type and convective state of thunderclouds, *J. Geophys. Res.*, *94*, 13 213–13 220, doi:10.1029/JD094iD11p13213.

Williams, E. R., B. Boldi, A. Matlin, M. Weber, S. Hodanish, D. Sharp, S. Goodman, R. Raghavan, and D. Buechler (1999), The behavior of total lightning activity in severe Florida thunderstorms, *Atmos. Res.*, *51*, 245–265.

Williams, E. R., V. Mushtak, D. Rosenfeld, S. Goodman, and D. Boccippio (2005), Thermodynamic conditions favorable to superlative thunderstorm updraft, mixed phase microphysics, and lightning flash rate, *Atmos. Res.*, *76*, 288–306, doi:10.1016/j.atmosres.2004.11.009.

Ziegler, C. L., D. R. MacGorman, P. S. Ray, and J. E. Dye (1991), A model evaluation of non-inductive graupel-ice charging in the early electrification of a mountain thunderstorm, *J. Geophys. Res.*, *96*, 12,833–12,855, doi:10.1029/91JD01246.

Zrnić, D. S., J. F. Kimpel, D. E. Forsyth, A. Shapiro, G. Crain, R. Ferek, J. Heimmer, W. Benner, T. J. McNellis, and R. J. Vogt (2007), Agile-beam phased array radar for weather observations, *Bull. Am. Meteorol. Soc.*, *88*, 1753–1766.